Engineering Structures 292 (2023) 116470

Contents lists available at ScienceDirect

Engineering Structures

journal homepage: www.elsevier.com/locate/engstruct

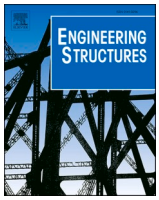

Experimental investigation of the behaviour of injection anchors in rubble stone masonry

Maria Pia Ciocci [a,b], Serena van Nimwegen [a], Arash Askari [a], Francesco Vanin [c], Paulo B. Lourenço [b], Katrin Beyer [a,*]

[a] Earthquake Engineering and Structural Dynamics Laboratory (EESD), School of Architecture, Civil and Environmental Engineering (ENAC), École Polytechnique Fédérale de Lausanne (EPFL), 1015 Lausanne, Switzerland

[b] Institute for Sustainability and Innovation in Structural Engineering (ISISE), Department of Civil Engineering, University of Minho, Campus de Azurém, 4800-058 Guimarães, Portugal

[c] Résonance Ingénieurs-Conseils SA, 1227 Carouge, Switzerland

ARTICLE INFO

Keywords:
Breakout failure
Digital image correlation
Injection anchors
Pull-out test
Rubble stone masonry
Strengthening
Wall-to-diaphragm connections

ABSTRACT

The seismic response of historical masonry buildings is largely controlled by the effectiveness of wall-to-diaphragm connections, which can be improved using injection anchors. Despite their use, there is a need for a better understanding of the performance of such anchoring system in stone masonry walls. This paper presents quasi-static pull-out tests performed on twelve specimens to investigate the behaviour of injection anchors in rubble stone masonry walls when breakout failure occurs. For each specimen, the experimental results are presented in terms of force–displacement curves, propagation of damage and crack pattern. It is shown that the anchoring details adopted in this study had a negligible influence on the pull-out force capacity of the anchoring system, while an increase in peak pull-out force was observed with increasing overburden stress applied. Because stone masonry specific capacity formulations have not yet been presented in the literature, the capacity is predicted using state-of-the art formulations for the pull-out load capacity of anchors installed in brick masonry. The limits of their applicability are discussed using the obtained experimental results.

1. Introduction

Unreinforced masonry (URM) buildings, which represent a significant portion of the building stock worldwide, are one of the most seismically vulnerable building typologies [1,2]. These buildings frequently collapse through the local out-of-plane overturning of facades or parts of facades. However, when the premature activation of such a failure mode is prevented, an integral structural behaviour can develop with an associated global mechanism which allows exploiting the capacity of in plane walls [3,4]. In this case, existing masonry buildings can sustain moderate to severe earthquakes. To prevent the overturning mechanisms, adequate in-plane diaphragm stiffness and efficient wall-to-diaphragm connections are required, keeping load well distributed among resisting elements [5].

In historical masonry buildings with timber floors, the floor beams are supported either directly on the wall or on a spreader beam embedded in the wall. If the floor beams have not been anchored to the wall, the force transfer between the floor beams and support relies only on friction, making the beams susceptible to sliding [6]. Mean and design values for the friction coefficient between timber and timber (for different surface qualities) and between timber and mortar have been determined experimentally [6,7]. In recent numerical simulations [8,9], this friction mechanism between the floor beams and support has been modelled explicitly, showing that only strengthening the diaphragm does not often improve behaviour and that an efficient transfer of forces from the diaphragm to the walls is necessary to achieve a global building response.

A common intervention technique for improving wall-to-diaphragm connections uses post-installed injection anchors composed of steel rods injected in pre-drilled holes in the substrate masonry material. In some cases, this system can also include a flexible fabric sleeve encasing the anchor rod and the injection material [10,11]. Threaded stainless-steel rods have been widely used, and fibre-reinforced polymer bars (FRP) and stainless–steel-reinforced polymer fabrics have also been adopted in

* Corresponding author.
E-mail addresses: mariapiaciocci@gmail.com (M.P. Ciocci), serena.evn@gmail.com (S. van Nimwegen), arashaskari@gmail.com (A. Askari), francesco.vanin@resonance.ch (F. Vanin), pbl@civil.uminho.pt (P.B. Lourenço), katrin.beyer@epfl.ch (K. Beyer).

https://doi.org/10.1016/j.engstruct.2023.116470
Received 29 January 2023; Received in revised form 5 May 2023; Accepted 9 June 2023
Available online 10 July 2023

recent systems [12]. A variety of injection materials have been used for this anchoring system, such as lime- or cement-based mortars and epoxy resin adhesive.

Anchoring systems injected with epoxy resin have been widely adopted for its easy installation (e.g. short-term curing to attain resistance and high viscosity for injection) [13,14]. They are typically installed horizontally in the perpendicular direction with respect to the wall (i.e. straight anchors) or inclined in the vertical plane [15], and anchors inclined in the horizontal plane may also be implemented by practitioners, aiming at involving more stones in the failure mechanism. When adopted for the strengthening of historical structures, their use requires to be carefully evaluated according to conservation principles and based on comprehensive scientific data obtained from experimental tests [16]. Despite their widespread use, only limited research has been conducted on injection anchors in stone masonry such that not much is known about their performance, as is also highlighted in post-earthquake assessments [17,18]. As a result, there is a need for a better understanding of this anchoring system.

Past studies have mainly investigated the behaviour of injection anchors in brick masonry [10,15,19–25], and very few experimental data are available for rubble stone masonry [11,26] and natural stones [13,14,27]. Based on these studies, several modes of failure are possible for injection anchors in masonry, which depend on a number of parameters: the properties of the materials involved in the system, the dimension and layout of the anchorage, masonry typology, installation methodology, support conditions, confinement effects and existing damage. Typical failure modes of injection anchors subjected to tensile loading are [14]:

- Masonry cone breakout failure;
- Bond (or pull-out) failure for slippage at the masonry-injection material interface;
- Bond (or pull-out) failure for slippage at the rod-injection material interfaces;
- Combined cone-bond failure;
- Tensile failure of the anchor rod;
- Pull-out failure of the unit (i.e. brick or stone) in which the anchor is embedded;
- Splitting failure in the unit or masonry at the anchor location.

Currently, no specific code provisions are available for injection anchors in historic stone masonry, so their use has been based mainly on provisions available for anchors injected in other masonry typologies. According to these provisions, the anchor design resistance should be assumed as the minimum pull-out force capacity associated with each expected failure after applying suitable safety factors. Nevertheless, with the exception of the Masonry Standards Joint Committee (MSJC) Code [28], current building codes and guidelines do not provide strength formulas for most of the expected failure modes, such as breakout failure [29]. In Europe, these guidelines are currently prescribed by the European Organisation for Technical Assessment (EOTA) [30–32]. In the literature, some formulations are available for predicting the pull-out load capacity of anchors injected in masonry under breakout failure that are based on models originally conceived for fastenings in concrete (for a review, see [12,33]). However, they consist of semi-empirical equations calibrated using tests performed on anchors installed in brick masonry, and their applicability to injection anchors in stone masonry is still in question.

To address these concerns, this paper presents an experimental programme of quasi-static pull-out tests on twelve specimens carried out at the École Polytechnique Fédérale de Lausanne (EPFL). The primary aim was to investigate the behaviour of anchors injected with epoxy in double-leaf stone masonry walls when masonry breakout failure occurs. To investigate the influence of the anchoring detail and the presence of a joist pocket in the masonry, three different configurations were considered. Moreover, the effect of applied vertical loading was also investigated in this study. In addition to traditional measurement systems, this experimental programme also adopted a three-dimensional (3D) optical measurement system that used Digital Image Correlation (DIC) to record the global response of the specimens.

The paper is organised in four sections. Section 2 presents the experimental test programme, including a description of the specimens, material properties, test setup, instrumentation, procedure and loading protocol. In Section 3, the experimental results obtained from the pull-out tests are presented in terms of force–displacement curves and damage. Then, the main findings regarding the influence of the investigated parameters are discussed by comparing the results obtained for all testing series. Finally, Section 4 uses the obtained experimental results to discuss the applicability of the formulas currently available to predict the pull-out force capacity of anchors installed in masonry.

2. Experimental programme

The experimental programme consisted of quasi-static pull-out tests on twelve specimens. Each specimen implemented an anchoring system composed of a pair of steel threaded rods injected in a double-leaf stone masonry wall with epoxy resin adhesive. Three different specimen configurations were considered, as illustrated in Fig. 1. In the first configuration, the anchors were straight and parallel to each other (labelled: PA), and in the second configuration, anchors were inclined at an angle (β) of 23° in the horizontal plane (labelled: IA). To investigate the presence of a joist pocket in the masonry, the third configuration had a timber joist placed next to two parallel anchors (labelled: PAT). Per specimen, the main parameter varied was the vertical loading on the masonry wall.

The specimens are described in terms of geometry, material and construction details in Section 2.1. Section 2.2 presents the mechanical characterisation tests carried out on the masonry constituents—lime-based mortar and limestones. For the mechanical properties of the masonry as a composite, the results obtained by Rezaie et al. [34] from simple compression and diagonal compression tests are applicable, since the same materials and construction technique were adopted. Sections 2.3 and 2.4 describe the test setup, procedure and loading protocol. Section 2.5 presents the instrumentation, consisting of hard-wired instruments and a 3D optical measurement system.

2.1. Description of the test specimens

All tested specimens were constructed as double-leaf stone masonry, with dimensions of 900 mm × 900 mm × 300 mm ($H_w \times L_w \times t_w$), as shown in Fig. 1. The two leaves were built using irregular dark limestone units measuring between 100 and 300 mm in length, with large pebbles used to fill the gaps. The mortar was prepared by mixing a commercial natural hydraulic binder, washed and dried sand (grain size: 0–3 mm) and gravel (grain size: 3–8 mm) in a ratio of 1:2.5:1 by volume. The water content of the mortar was chosen to achieve the optimum workability of the mixture.

The anchoring system consisted of a pair of galvanised steel threaded rods (steel class 8.8) injected in the wall using a two-component epoxy resin. For all specimens, the system was installed at mid-height of the wall with an embedment length (l_e) of 250 mm. The rods had a diameter (d) of 16 mm and were spaced apart by $s = 140$ mm (centre to centre), as shown in Fig. 1. As per the manufacturer's recommendations, a 20-mm borehole diameter (d_0) was adopted for the selected rod diameter, and the borehole passed through the entire thickness of the walls to allow the installation of instrumentation at the rod ends.

Each wall was constructed on a 35–mm-thick steel plate. To increase the friction between the plate and wall base, the surface of the plate was roughened by a thin layer of sand and epoxy, and a timber formwork was used to maintain the correct dimensions and verticality during their construction (Fig. 2). For PAT specimens, the timber joist was positioned when the wall was built to 500 mm and then was surrounded by mortar

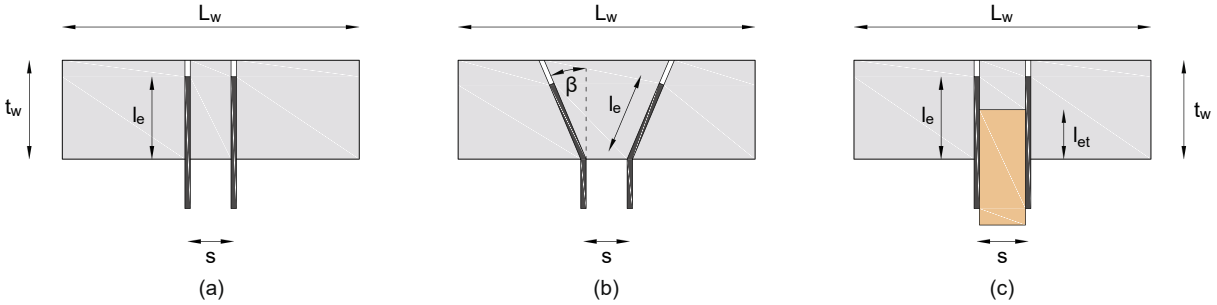

Fig. 1. Testing series: (a) PA specimens; (b) IA specimens; (c) PAT specimens. Note that $L_w = 300$ mm, $t_w = 300$ mm, $l_e = 250$ mm, $l_{et} = 150$ mm, $s = 140$ mm and $\beta = 23°$.

Fig. 2. Construction of the masonry walls.

and stones. The timber joist had a cross-section of 140 mm × 200 mm, and its embedment length was equal to half of the wall thickness (l_{et} = 150 mm).

The walls were left to set for 28 days post construction under laboratory conditions, and then the holes for the anchors were cored with a diamond tipped rotary drill, limiting vibrations to prevent damage to the specimens. For all specimens, the holes were cored according to the designated layout, whether it was stone or mortar at the drill site. To ensure the horizontality of the holes, the drill was mounted on a concrete block. Particular care was given to cleaning the holes and injecting the epoxy, which can significantly influence anchor performance. Since no official provisions exist for installing injection anchors in historic rubble stone masonry, the manufacturer's recommendations were followed with some minor adjustments.

The cleaning procedure included flushing the hole with water two times to suspend and remove particles, brushing the interior of the hole two times with a nylon bristle brush, then flushing it with water twice again. Water was flushed at a pressure sufficient to wash away any debris while avoiding damage to the boreholes. The holes were then dried twice using an air pistol, brushed twice to remove debris, and again injected with air two times. The amount of epoxy injected into standard concrete or material without voids is usually recommended to be 2/3 of the embedment length. In this case, the holes were filled for 3/4 of the length using a hose and piston such that the small amount of pressure could facilitate filling the voids in contact with the borehole. This allowed the excess epoxy to flow forward toward the mouth of the hole when the rod was inserted. To obtain an optimum bond over the entire embedment length (i.e. 250 mm) and to ensure the horizontality of the anchors, the following procedure was followed. Expanded polystyrene cylinders were placed at the back of each borehole before the anchor injection to prevent that the epoxy could flow out from the back of the borehole. They were carefully removed after the epoxy resin had cured. To ensure the correct location of the anchors while inserting the rods, timber elements and a laser level were used.

Until immediately before testing, the timber joists used for the PAT specimens were supported to prevent any rotation due to their weight (Fig. 3a). However, damage was still observed in these specimens before testing, possibly due to shrinkage and expansion of the masonry walls and timber joists. For all PAT specimens, a well-defined crack occurred from the top of the joist pocket up to the top face of the wall where the crack then crossed the entire wall thickness, with a maximum width of about 5 mm (Fig. 3b). Barring the first specimen, the existing cracks in the PAT specimens were repaired via grout injection before performing pull-out tests.

The crack repair was carried out using a high-fluidity grout prepared with a commercial pre-mixed hydraulic binder used for the consolidation of historic rubble stone masonry. The grout injection procedure was defined following the manufacturer's recommendations and suggestions provided in previous studies (e.g. [35,36]). A series of 5–mm-diameter holes was made in the width of the existing crack to place flexible plastic tubes along the crack length. The location of the tubes was adapted for each wall according to the shape of the crack, and they were generally spaced apart by 50–100 mm. Before the injection, the cracks were sealed on the masonry wall surface to prevent the grout from seeping out, and water was flushed through the tubes to avoid excessive water absorption after grouting. The grout injection was carried out via syringes, starting from the tubes placed at the bottom of the crack. When the grout seeped out from the higher adjacent tube or when it was not possible to inject more material, the injection was stopped and continued from the adjacent tube. The injection was carried out to attempt to fill the existing crack at the top of joist without excessive grouting spread in the masonry wall.

2.2. Material properties of the masonry constituents

2.2.1. Mortar

Samples collected from each batch of mortar during wall construction were tested according to EN 1015–11 [37] to determine the flexural tensile and compression strengths. Three-point bending tests were carried out on prisms with dimensions of 160 mm × 40 mm × 40 mm, and

Fig. 3. PAT specimens: (a) construction; (b) existing crack (back view of the wall).

uniaxial compression tests were performed on the specimen halves generated from the flexural tests. The tests were performed under load control, with a constant loading rate of 10 N/s for flexural and 100 N/s for compression. Table 1 summarises the mean strength values and the coefficients of variation (CoV) obtained one year after the samples were cast, at about the time the pull-out tests were performed. The curing conditions of the mortar samples were the same as the wall specimens, i.e. under laboratory conditions. The mean values obtained for the flexural tensile strength (f_{ft}) and compression strength (f_c) were 0.91 MPa and 4.34 MPa, respectively. The significant level of dispersion observed can be attributed to the different water contents in preparing the mortar.

2.2.2. Limestones

To characterise the compressive strength and elastic properties of limestone, uniaxial compression tests were performed on four samples prepared using cores drilled from the units used to construct the masonry walls. As recommended by the ASTM D7012-14 [38], the specimens had a length to diameter ratio equal to 2.0. Because the stones were rather small, a diameter smaller than the minimum specimen diameter recommended was adopted. Therefore, the specimens had an average diameter of 23.6 mm and an average height of 50.5 mm. The cores were oriented perpendicular to the stone bedding planes. The compression tests were carried out under displacement control at a constant loading rate of 1 μm/s, resulting in failures within 2 and 15 min of testing, as suggested by the ASTM D7012-14 [38]. The longitudinal deformation was recorded by two linear variable differential transformers (LVDTs) placed 180° apart between the lower and upper steel plates, while a circumferential ring was installed at mid-height of the specimens to measure the transversal deformation. Table 2 presents the values of the compression strength (f_c), modulus of elasticity (E) and Poisson's ratio (ν), obtained following the ASTM D7012-14 guidelines [38], where E was calculated as the tangent modulus of the stress–strain curve at a stress level of 50 % of the maximum strength. As shown in Fig. 4, the specimens failed depending on their microstructure, mostly by axial splitting.

Table 1
Results of material tests on the mortar used to construct the masonry walls.

Specimen name	f_{ft} [MPa]	f_c [MPa]
PA1	0.74 (30 %, 9)	3.86 (30 %, 9)
PA2	1.10 (27 %, 7)	5.53 (16 %, 7)
PA3	1.11 (18 %, 7)	5.59 (13 %, 7)
PA4	0.82 (30 %, 7)	4.09 (28 %, 7)
IA1	1.06 (28 %, 9)	5.23 (19 %, 9)
IA2	1.01 (21 %, 7)	4.80 (18 %, 7)
IA3	0.76 (41 %, 9)	3.15 (37 %, 9)
IA4	1.11 (27 %, 7)	4.95 (22 %, 7)
PAT1	1.01 (39 %, 6)	4.50 (45 %, 6)
PAT2	0.78 (22 %, 9)	3.64 (28 %, 9)
PAT3	0.74 (25 %, 7)	3.72 (26 %, 7)
PAT4	0.66 (42 %, 8)	3.21 (43 %, 8)
Total	0.91 (35 %, 92)	4.34 (33 %, 92)

Notation: Mean value (CoV, number of samples).

Table 2
Results of uniaxial compression tests on limestone specimens.

Specimen name	f_c [MPa]	E[GPa]	ν[-]
UCS1	134.1	31.1	0.08
UCS2	107.6	26.5	–
UCS3	116.4	23.8	0.10
UCS4	106.1	26.4	0.07
Total	116.1 (11 %)	27.0 (11 %)	0.08 (18 %)

Notation: Mean value (CoV).

2.3. Test setup

The test setup used to perform the pull-out tests is shown in Fig. 5. Each masonry wall was placed between two 360–mm-high steel profiles in a universal testing machine that applied the axial loading during the test. The machine had a mobile hydraulic piston at the base (with ±125 mm stroke and +2.5/−10 MN force capacity) and four load cells at the top. Steel plates prepared with a layer of sand and epoxy were placed at the top and at the bottom of the walls. Out-of-plane displacements of these steel plates were prevented by means of an L-shaped steel profile and bolted connections. To guarantee uniform stress transfer upon vertical load application, a cement-based mortar layer was applied at the top surface of the wall for the PA specimens. Based on the results obtained from these tests (Section 3.1), this layer was subsequently made of epoxy resin for the IA and PAT specimens to avoid sliding at the top of the wall. The rotation of the steel profile at the top and bottom of the wall was prevented. The configuration adopted in this setup was therefore representative of fixed–fixed boundary conditions.

The pull-out load was applied to PA and IA specimens by connecting the anchors via bolts and hinges to a square box section profile, which in turn was connected to a long-threaded rod running through a 300 kN hydraulic jack and a load cell (Fig. 5a). For PAT specimens, two systems were installed in the test setup to guarantee the load transfer to the anchors: the load system and the so-called 'shoe system' (Fig. 5b). The former consisted of a C-shaped steel profile connecting the long rod with two L-shaped steel profiles, which in turn were bolted to the timber joist on the external sides. The latter shoe system implemented similar steel-to-timber connections, transferring the load to a stiffened L-shaped profile. As shown in Fig. 6, this profile was connected to the anchors via two box section profiles and a steel plate. A layer of cement-based mortar was placed between the L-shaped profile and the wall. Moreover, a vertical support was installed at the end of the timber joist to

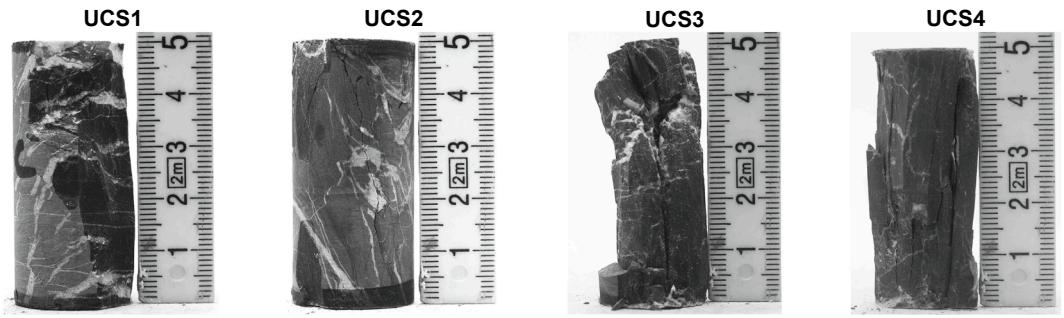

Fig. 4. Limestone specimens after failure.

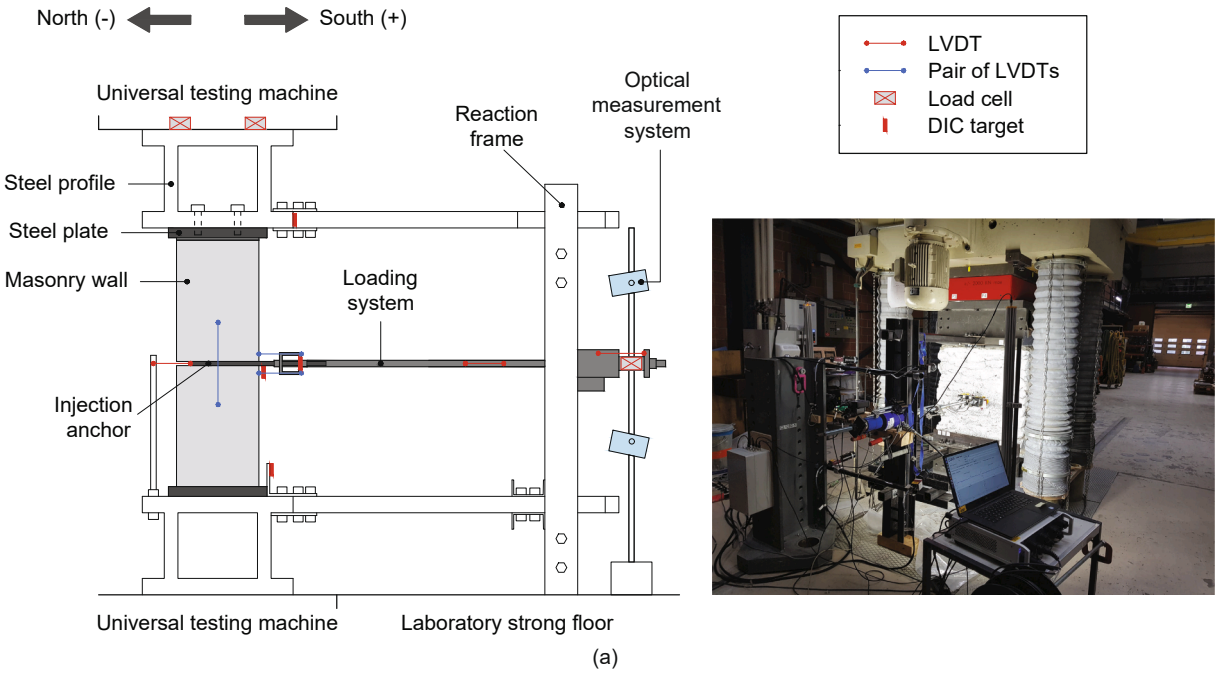

Fig. 5. Test setup and instrumentation used for the pull-out tests: (a) PA and IA specimens; (b) PAT specimens.

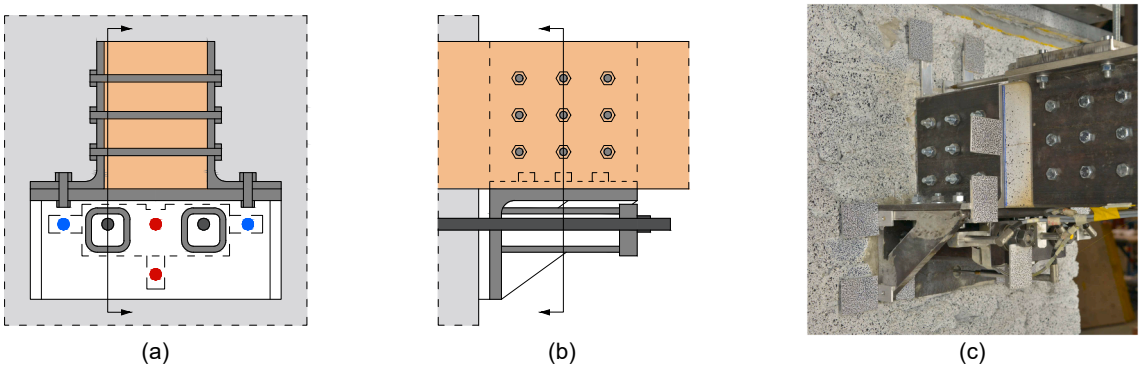

Fig. 6. Shoe system adopted for PAT specimens: (a) front view; (b) section; (c) photo.

prevent its excessive rotation, and a sliding system was placed to allow the joist to slide horizontally during testing.

2.4. Test procedure and loading protocol

The quasi-static pull-out tests were performed in two phases for all specimens. Each specimen was initially subjected to a vertical force (F_v) imposed by the piston at the base of the machine, which was operated in a displacement-controlled mode. In this phase, unloading–reloading cycles were conducted to reach the prescribed F_v value, which was changed per test to investigate the influence of the vertical overburden stress (σ_v), i.e. the ratio between the prescribed vertical force and the nominal cross-section of the wall (300 mm × 900 mm). As a result, the adopted value of σ_v ranged between 0.10 and 0.30 MPa.

In phase two, the horizontal force (F), i.e. pull-out load, was applied using the hydraulic jack. Here, the testing machine was operated in a force-controlled mode, and the vertical force was generally kept constant (see Section 3). For all specimens, unloading–reloading cycles were carried out in which F was increased by 10 kN between cycles until the peak pull-out force (F_{max}) was reached. All the specimens were tested until there was a drop of approximatively 80 % with respect to the obtained F_{max}, with the exception of some specimens discussed in Section 3.

2.5. Instrumentation

The adopted hard-wired instrumentation consisted of load cells and LVDTs. Load cells in the universal testing machine measured the vertical load applied to the masonry wall, and the pull-out force was measured by a load cell placed behind the hydraulic jack. For PAT specimens, the vertical force at the support system of the timber joist (F_{vs}) was also measured. As shown in Fig. 5, the LVDTs were placed at several locations of the setup, including at the front and at the back of the anchors. The former LVDTs were installed to measure the out-of-plane displacements of the masonry wall with respect to the profile connecting the anchors, and the latter measured the slippage of the anchors with respect to the lower steel profile fixed at the testing machine. For all the specimens, the LVDTs behind the anchors were installed along the axis of the anchors. For PA and PAT specimens, only one anchor was instrumented per specimen (i.e. the anchor on the east side of the wall), while for IA specimens, LVDTs were installed on both anchors.

In addition, the setup adopted a 3D optical measurement system that used the DIC to measure displacements on the front face of the specimens. For this reason, the front face was painted in white, and black speckles were randomly sprayed onto it ensuring appropriate speckle dimension and density. As shown in Fig. 5, additional speckled patches were also glued at specific locations of the setup, such as on the steel profiles and the anchors. The optical measurements were recorded by two stereo-camera systems that were placed symmetrically with respect to the anchoring system. Before testing, the cameras were calibrated using a standard calibration target plate, and care was paid to guarantee that the wall surface was lit appropriately. To compute the 3D displacement field, the acquired high-resolution grey-scale images were analysed in the software VIC-3D version 8.2.4 [39].

3. Experimental results

For all specimens, the force–displacement curve was constructed using the pull-out force (F) exerted by the horizontal hydraulic jack versus the horizontal displacement (Δ) recorded by the LVDTs placed behind the anchors. In these curves, the vertical forces F_v and F_{vs} are also reported here. To identify trends between the specimen configurations, key parameters of the force–displacement curves are tabulated, namely: the pull-out load-bearing capacity (F_{max}), the corresponding value of displacement $[\Delta_{Fmax} = \Delta(F_{max})]$, and the displacement value computed when the pull-out load dropped to 80 % of the maximum value $[\Delta_{0.8\,Fmax} = \Delta(0.8\,F_{max})]$. For the PAT specimens, the vertical force recorded at the support of the timber joist when the F_{max} was reached is also provided $[F_{vs,\,Fmax} = F_{vs}(F_{max})]$.

The failure mode of the specimens was evaluated based on visual observation during their testing and demolition. The progression of damage was quite complex for each specimen. The obtained failure mechanism mobilised a large number of mortar joints and stones within the pulled area on the wall front face, and plotting the observed crack pattern does not contribute to a better understanding of the failure mode. Nevertheless, the DIC measurements allowed to analyse the deformed shape of the specimens during testing. Hereby, the DIC displacement field component calculated in the out-of-plane (OOP) direction with respect to the wall front surface is presented for representative tests, at steps indicated in the corresponding force–displacement curve. These steps were selected when the maximum pull-out load was reached or when the displacement recorded behind the anchors was about 10–15 mm.

This section first describes the experimental results for each of the three series in terms of force–displacement curves, propagation of damage and crack patterns (Sections 3.1–3.3). Further details on the test procedure and loading protocol adopted for each specimen are also provided. Afterwards, the experimental results between testing series are compared, and the influence of the investigated parameters—anchoring detail, joist pocket and overburden stress—is discussed in Section 3.4.

3.1. Specimens with parallel anchors (PA)

3.1.1. Force-displacement response curves

Specimens PA1 and PA2 were tested under the lowest value of F_v adopted in this experimental programme, corresponding to σ_v = 0.10 MPa. Test PA1 had to be stopped prematurely due to sliding of the

wall, and hence it is not valid. For specimen PA2, a value of F_{max} = 42.4 kN was obtained. After F_{max} was reached for PA2, a technical issue switched the testing machine from a force-control to displacement-control mode (Fig. 7a). As a result, the vertical force F_v and hence also the pull-out force F increased; F_v was 45.2 kN when the pull-out force reached its maximum value of 53.2 kN. In the tests of PA3 and PA4, the F_v value was increased to 54.0 kN (σ_v = 0.20 MPa) to investigate the effect of the vertical load on the pull-out resistance. The force–displacement response for these specimens showed a near-linear branch before F_{max} was reached and a significant decrease in force with increasing displacement in the post-peak behaviour (Fig. 7b and c). The F_{max} values were calculated as 50.3 kN and 57.1 kN for PA3 and PA4, respectively (Table 3).

3.1.2. Propagation of damage and crack pattern

For specimen PA2, no cracking on the masonry surface could be visually observed when F_{max} was reached. However, the DIC results allowed to identify the imminent development of a horizontal crack at the mid-height of the wall, as evidenced in Fig. 8a. A rapid propagation of cracks in the masonry was observed for specimens PA3 and PA4 when the post-peak branch initiated, mainly developing through the mortar and mortar-stone interface. For specimen PA3, cracks surrounded the anchors in the lower part of the wall, and two cracks also developed from the anchoring area to the top of the wall. Specimen PA4 showed cracking around the anchoring zone and diffuse damage in the surrounding area, as reflected by the DIC results in Fig. 8b. Cracks radiating from the anchors to the wall corners were also observed. While demolishing PA4, well-defined fracture surfaces were observed, angled at approximately 45° in the vertical plane and 55–60° in the horizontal plane (Fig. 9a and b). Moreover, presumably as a result of their proximity, there was an overlap between the masonry breakout blocks that developed around each anchor. Notably, the stones into which the free ends of the anchors were injected cracked, and the masonry failure block had a depth equal to the embedment length of the anchors (Fig. 9c).

3.2. Specimens with inclined anchors (IA)

3.2.1. Force-displacement response curves

To have a consistent comparison with the previous tests, a value of F_v = 54.0 kN was adopted for the first three IA specimens, corresponding to σ_v = 0.20 MPa (Table 4). The average value of F_{max} obtained for these specimens was 54.1 kN (CoV = 4 %). Once F_{max} was reached, there was a sharp decrease in pull-out load with increasing displacements for these specimens, as shown in Fig. 10. It is to be noted that a drop in the pull-out force occurred at the final reloading for specimen IA1 (Fig. 10a). This is due to the fact that the box section profile connecting the anchors rotated causing a horizontal misalignment of the long bar from the OOP direction of the wall. For specimen IA2, the rotation was significant, and the test had to be stopped before the pull-out load dropped below 80 % of the maximum value (Fig. 10b). In consequence, the test setup was improved, and the rotation of the box section profile was prevented in tests IA3 and IA4.

Table 3
PA specimens: applied vertical load and obtained force and displacement capacities. Note that masonry breakout failure occurred for all specimens.

Specimen	F_v [kN]	σ_v [MPa]	F_{max} [kN]	Δ_{Fmax} [mm]	$\Delta_{0.8\,Fmax}$ [mm]
PA2	27.0 (45.2)*	0.10	42.4 (53.2) *	0.74 (2.29) *	–
PA3	54.0	0.20	50.3	1.14	4.92
PA4	54.0	0.20	57.1	2.35	5.53

()* Values obtained after the testing machine switched to a displacement-control mode.

To gain additional information from specimen IA4, the value of F_v was varied while applying the pull-out load, as shown in Fig. 10d. The F_v value was initially adopted to be 81.0 kN (i.e. σ_v = 0.30 MPa), and a value of F_{max} = 64.9 kN was obtained. Then, the vertical loading was decreased to 54.0 kN in the second loading cycle of the post-peak branch, and it was finally increased to 108.0 kN in the third cycle. Fig. 10d shows that the first change in F_v caused a drop in F of approximately 10 kN, while no significant effects were observed in the force–displacement curve when F_v was increased in the last loading cycle.

3.2.2. Propagation of damage and crack pattern

After F_{max} was reached for specimen IA1, cracking occurred mainly in one side of the wall, as also reflected by the high OOP displacements shown in Fig. 11a. For this specimen, cracking initiated near the east anchor and propagated in a radial pattern towards the east side of the wall. A well-defined crack was observed at the mid-length of the wall, extending from the anchoring zone to the top of the wall. While extensive damage was observed on the east front face, including to the stones, thin cracks were observed in mortar joints and at the mortar-stone interface on the west front face of the wall. At the end of the test, splitting cracks were also observed in the wall thickness on the east side, suggesting the separation of the masonry leaves, which was indeed confirmed during demolition (Fig. 12a). The masonry failure block that developed around the east anchor suffered such extensive damage that its measure could not be reliably recorded. On the other side, a well-defined masonry block was observed. Similar observations were also made for specimen IA2, with the west side of the wall containing the

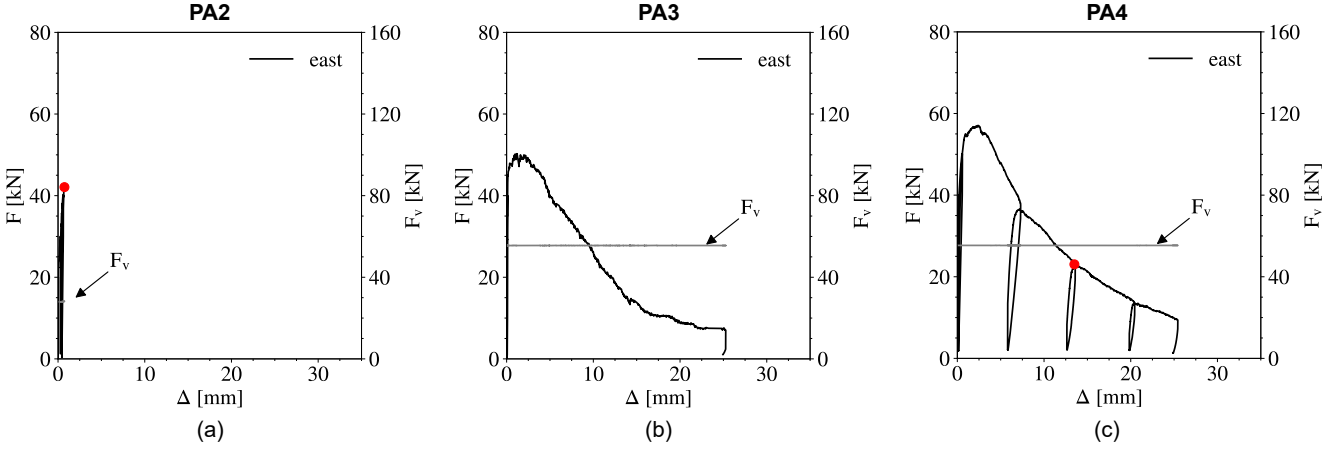

Fig. 7. Force-displacement curves obtained for PA specimens: (a) PA2; (b) PA3; (c) PA4. The red circles mark the step for which the DIC results are plotted in Fig. 8. (For interpretation of the references to colour in this figure legend, the reader is referred to the web version of this article.)

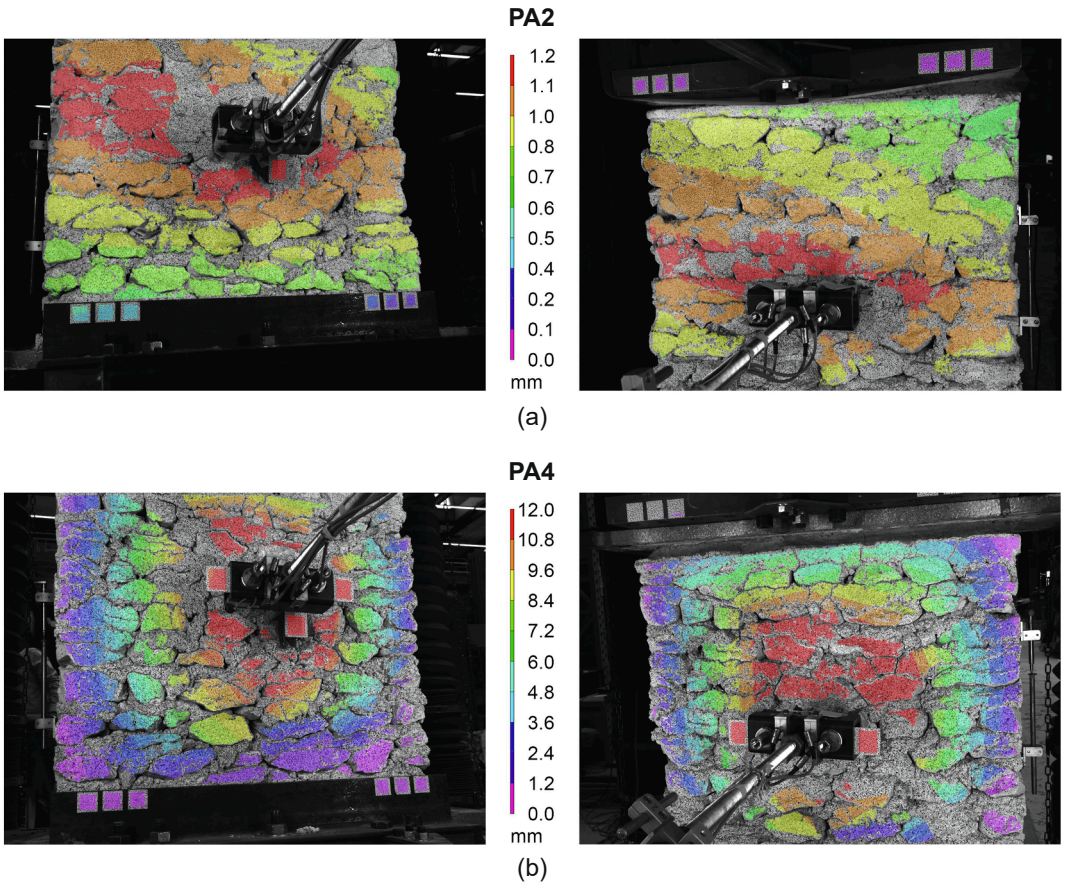

Fig. 8. OOP displacements for PA specimens at the steps indicated in Fig. 7: (a) PA2; (b) PA4.

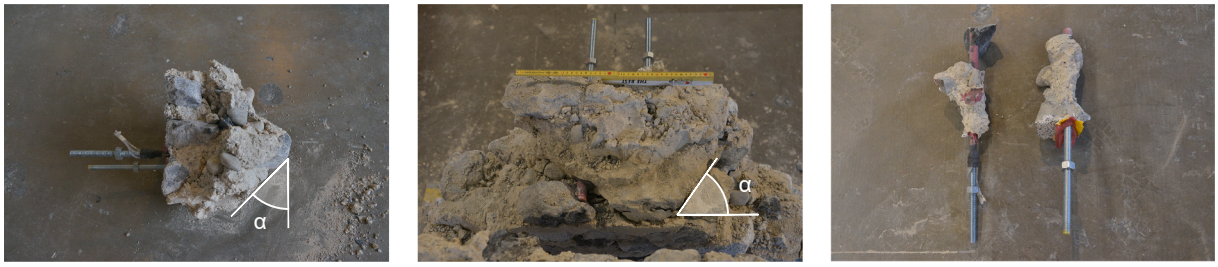

Fig. 9. Damage observed for PA4 specimen after demolition: (a) lateral view of the masonry breakout block; (b) top view of the masonry breakout failure; (c) state of the anchors.

Table 4
IA specimens: applied vertical load and obtained force and displacement capacities. Note that masonry breakout failure occurred for all specimens.

Specimen	F_v [kN]	σ_v [MPa]	F_{max} [kN]	Δ_{Fmax} [mm] *	$\Delta_{0.80\,Fmax}$ [mm] *
IA1	54.0	0.20	51.7	0.89, 0.93	5.94, 4.19
IA2	54.0	0.20	55.5	0.66, 1.28	5.08, 7.24
IA3	54.0	0.20	55.1	0.93, 1.05	5.21, 5.11
IA4	81.0	0.30	64.9	0.86, 0.90	6.48, NaN

*East, west.

most damage.

For specimens IA3 and IA4, a fairly symmetrical distribution of OOP displacements with respect to the anchoring system was observed on the front wall surface, resulting in a similar damage propagated in the east and west sides. Fig. 11b shows the DIC results obtained for IA3. For these specimens, the anchoring system was surrounded by cracking, and radial cracks developed outwards. Moreover, cracks between the masonry leaves were also visible on the external surface of the wall at the end of testing, especially for specimen IA4 where the crack on the east side reached a significant width (>1 cm). Splitting cracks also occurred between the two anchors for these specimens. The masonry failure blocks formed along the full embedment length of each anchor and their overlapping was clearly visible during their demolition. Fig. 12b and c show the breakout failure that was observed for specimen IA3, which was characterised by an angle of approximately 45° in the vertical plane. In the horizontal plane, an angle of 30° was measured on the west side, while a 60° angle was observed on the east side where no splitting cracking occurred between the masonry leaves.

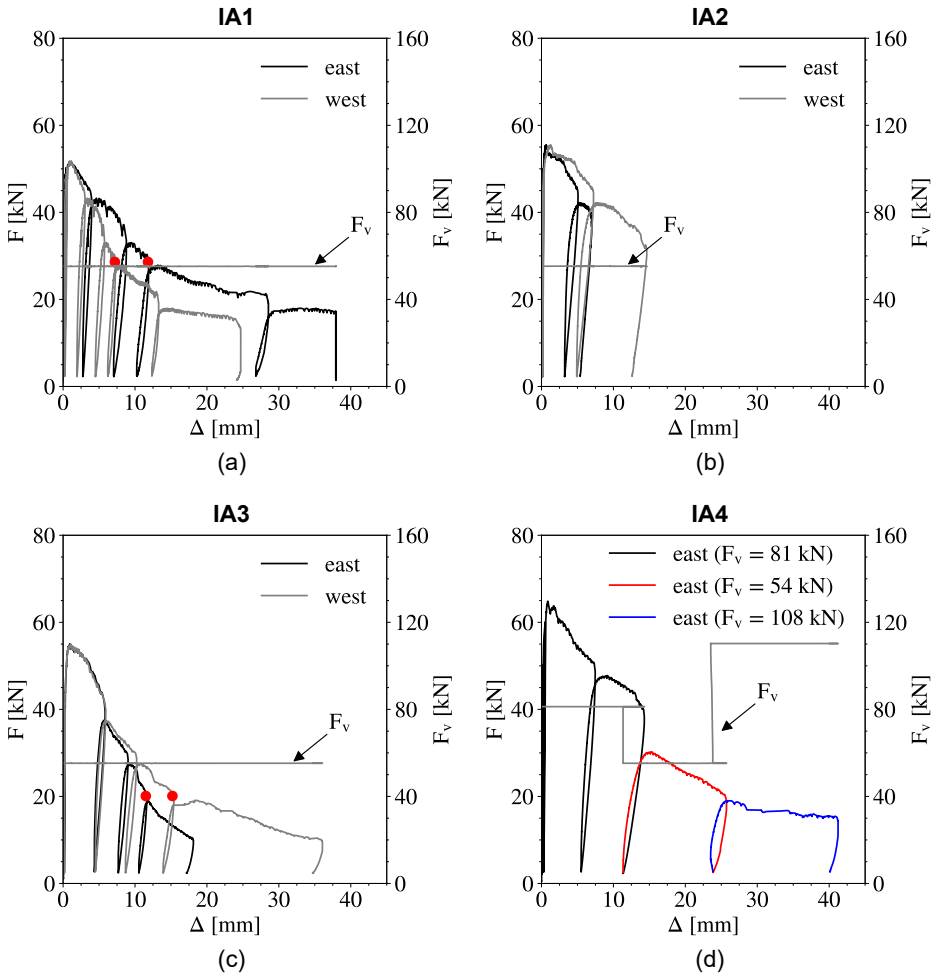

Fig. 10. Force-displacement curves obtained for IA specimens: (a) IA1; (b) IA2; (c) IA3; (d) IA4. The red circles mark the step for which the DIC results are plotted in Fig. 11. (For interpretation of the references to colour in this figure legend, the reader is referred to the web version of this article.)

3.3. Specimens with parallel anchors and timber joist (PAT)

3.3.1. Force-displacement response curves

As described in Section 2.1, damage was observed in the PAT specimens before testing. PAT1, which had less extensive existing damage when compared to the other PAT specimens, was tested without the crack repair. Despite the existing damage, the force–displacement curve behaved similarly to previous tests (Fig. 13a), and the obtained value of F_{max} was 60.9 kN. However, there seems to have been some influence from the existing damage, as suggested from measurements recorded at the end of the vertical loading phase by the load cells in the universal machine and the DIC results. For this reason, crack repair was carried out for the other PAT specimens.

PAT2 was tested under the same vertical loading as PAT1, corresponding to $\sigma_v = 0.20$ MPa. As shown in Table 5, the F_{max} value obtained for this specimen was 25 % higher than that obtained for PAT1. For PAT3, a value of $F_v = 27.0$ kN was adopted ($\sigma_v = 0.10$ MPa), and the obtained F_{max} was 41.9 kN. PAT4 was tested under a vertical loading of 81.0 kN (i.e. $\sigma_v = 0.30$ MPa), resulting in a maximum pull-out load of 57.4 kN. For this test, the force–displacement curve showed less of a decrease in force with an increasing displacement during the last loading cycle (Fig. 13d). This may be related to the sliding of the masonry portion of the wall involved in the failure mechanism, as discussed in the following section.

3.3.2. Propagation of damage and crack pattern

While testing PAT1 and PAT2, the OOP displacements of the front face of the masonry wall progressively increased with a rather symmetrical distribution. Fig. 14a shows the DIC results obtained for PAT1 when F_{max} was reached. In the post-peak branch, diagonal cracks propagated in these specimens from the top corners of the joist pocket and the anchoring zone towards the top corners of the wall. Vertical cracking was also found in the wall thickness, especially for PAT1 where a crack with significant width was observed on the east side of the wall. In the lower part of the wall, cracks propagated from the anchors to the base and the bottom corners of the wall. While for PAT2 these cracks occurred on both wall sides, they were mainly observed on the east side for PAT1. Notably, damage was observed at the back face of the wall for PAT1 (Fig. 15a), while for PAT2 the stones in which the anchors were injected were found to be cracked during the demolition of the wall.

For PAT3 significant damage mainly occurred on the east side of the wall, as also reflected by the DIC results in Fig. 14b. Diagonal cracking propagated from the joist pocket to the top corner of the wall as well as from the east anchor to the lateral side of the specimen. Thin cracking in the wall thickness was also observed on the east side. When compared to the other PAT specimens, PAT3 had a breakout failure block significantly detached from the rest of the wall, as shown in Fig. 15b. For PAT4, a severe crack propagated vertically from the top-east corner of the joist pocket to the top of the wall, which was adjacent to the repaired crack. Widespread damage occurred on the west side of the wall, where a splitting crack with a significant width was observed in the wall thickness. Similar to other specimens, the demolition of PAT4 showed that the east anchor was injected in a large stone that had severely cracked. In contrast to the other specimens, the free end of the west

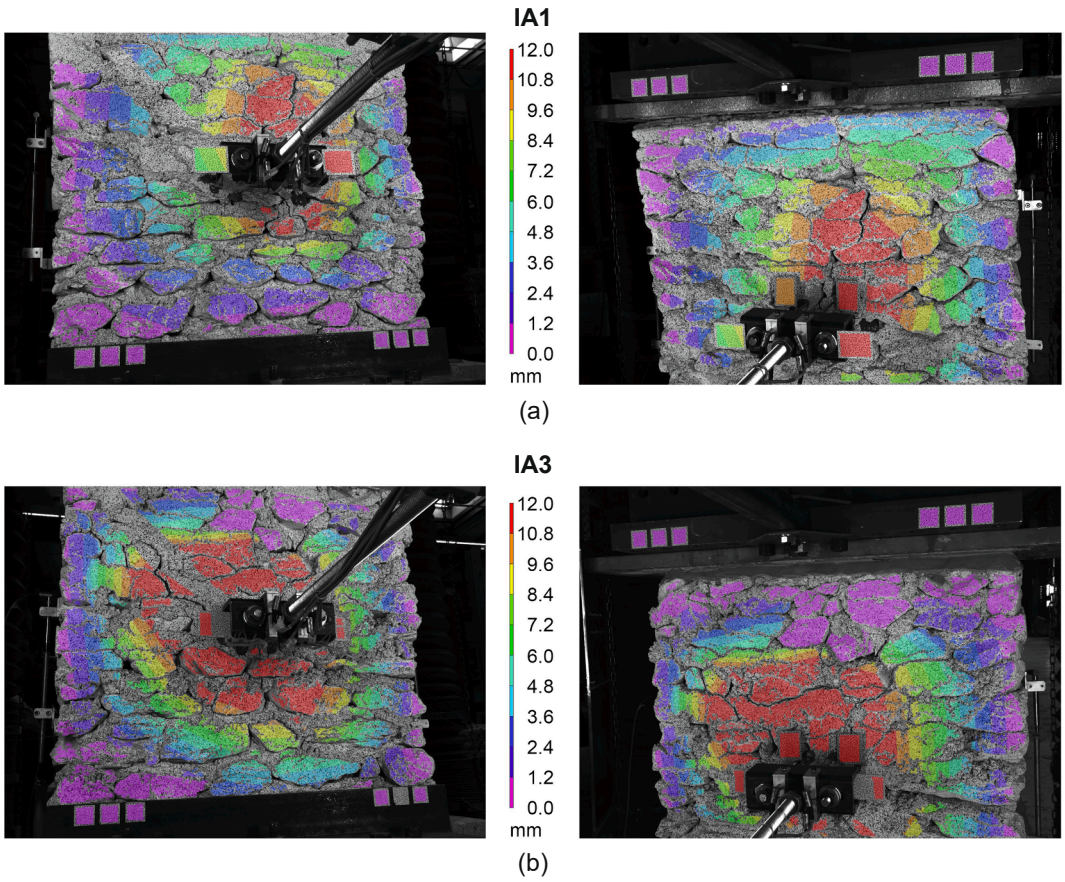

Fig. 11. OOP displacements for IA specimens at the steps indicated in Fig. 10: (a) IA1; (b) IA3.

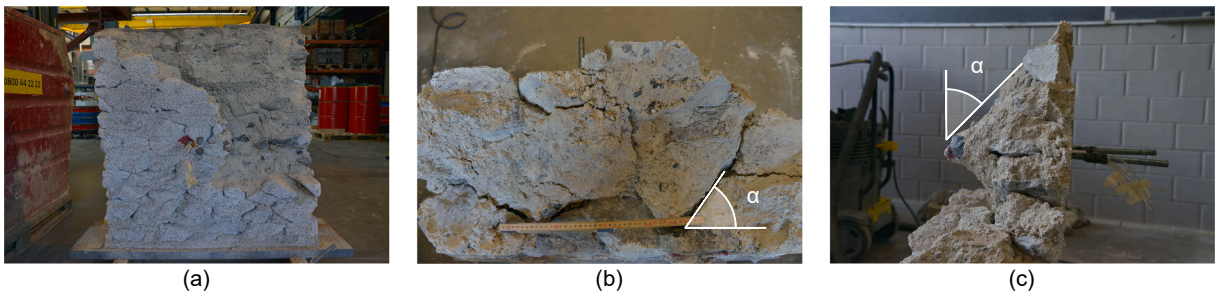

Fig. 12. Damage observed for IA specimens during demolition: (a) separation of masonry leaves (IA1); (b) top view of the breakout failure (IA3); (c) lateral view of the breakout failure (IA3).

anchor was embedded in mortar (Fig. 15c).

For all PAT specimens, breakout failure occurred, and the masonry blocks that formed around each anchor overlapped. Notably, the failure in these specimens involved the masonry portion surrounding the joist pocket (Fig. 16a), and significant damage occurred at the back face of the pocket, especially at the top (Fig. 16b). Behind the joist pocket, cracks were also found in the masonry leave at the back of the walls, as shown in Fig. 16c. As a result, the breakout failure block had a rather complex shape for these specimens. Regarding the timber beam embedded in the masonry, no damage was observed.

3.4. Discussion

For all specimens, the experimental force–displacement curves showed that the pull-out load increased almost linearly up to its maximum values. At F_{max}, relatively low values of displacement Δ_{Fmax} were calculated, indicating a stiff response of the structural system in the pre-peak branch. After F_{max}, there was a significant drop in force with increasing displacements. For the vertical loading values adopted in this study, the values of the peak pull-out force ranged from 41.9 kN to 75.9 kN (Fig. 17).

When a vertical overburden stress σ_v of 0.20 MPa was applied, the mean value of F_{max} was 53.9 kN with associated CoV of 5 %, calculated considering the PA and IA specimens. Based on these results, the anchoring detail did not considerably influence the peak pull-out force in this study. Due to the scatter in the results of the PAT specimens, it is not straightforward to establish the effect of the joist pocket on the peak pull-out load. Considering the results for PAT1 and PAT3, the pull-out load capacity was not drastically affected. The higher F_{max} obtained for PAT2 might be related to the grouting used to repair the crack, while the lower value for PAT4 may be due to the presence of pre-test damage.

The influence of the vertical loading on the peak pull-out force was

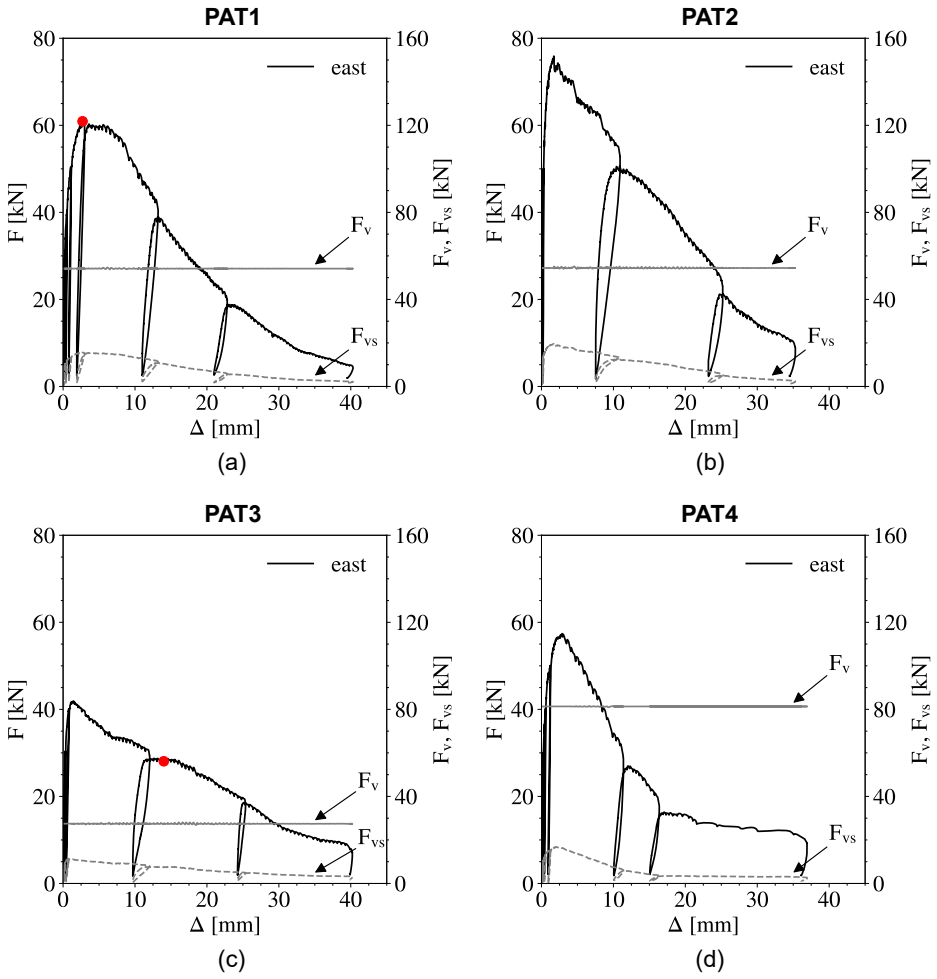

Fig. 13. Force-displacement curves obtained for PAT specimens: (a) PAT1; (b) PAT2; (c) PAT3; (d) PAT4. The red circles mark the step for which the DIC results are plotted in Fig. 14. (For interpretation of the references to colour in this figure legend, the reader is referred to the web version of this article.)

Table 5
PAT specimens: applied vertical load and obtained force and displacement capacities. Note that masonry breakout failure occurred for all specimens.

Specimen	F_v [kN]	σ_v [MPa]	F_{max} [kN]	$F_{vs,\ Fmax}$ [kN]	Δ_{Fmax} [mm]	$\Delta_{0.80\ Fmax}$ [mm]
PAT1	54.0	0.20	60.9	15.6	2.71	10.40
PAT2	54.0	0.20	75.9	19.5	1.72	8.32
PAT3	27.0	0.10	41.9	11.1	1.44	7.61
PAT4	81.0	0.30	57.4	16.3	2.86	6.69

clearly observed for the PA and IA specimens, as shown in Fig. 17. For these tests, the value of F_{max} increased linearly with an increasing overburden stress in this study ($R^2 = 0.89$). This trend was also observed in the post-peak behaviour of IA4. Notably, the 10 kN drop in F that occurred when the F_v value was decreased from 81 kN to 54 kN is similar to the increase in value of F_{max} that was obtained for this specimen when compared to IA specimens tested under $F_v = 54$ kN (Fig. 10). The increase in pull-out load capacity with increasing vertical loading was also confirmed by the results obtained for the PAT specimens except PAT4. Besides the possible presence of pre-test damage, this might also be related to the fact that the free end of the west anchor of this specimen was embedded in mortar rather than stone (see Section 3.3.2), resulting in a lower pull-out load resistance value.

The DIC results showed the development of the breakout failure on the wall front surface, with the highest OOP displacement values located in the masonry around the anchoring system and decreasing towards the wall edges. Reflecting the near-linear behaviour obtained in the force–displacement curves, no significant damage was visible in the masonry before reaching the peak pull-out force. Thereafter, a significant propagation of cracks occurred on the front face of the walls that rapidly grew in length, width and number. Also, after the peak pull-out force was achieved, a snap-back behaviour was recorded by the LVDTs placed at the front of the masonry walls, meaning that the bond between the injection anchors and masonry was no longer engaged in the full response of the specimens.

Despite the differences observed in the crack pattern of each specimen, there were some common features across the testing series. In general, there was cracking around the anchoring system, and cracks also developed from the anchoring area outwards. While these cracks developed horizontally towards the lateral sides in the specimens tested under the lowest vertical loading, they propagated diagonally towards the corners and edges of the walls when a higher vertical load was applied. Though some stones close to the wall corners were also cracked, cracking mainly developed through the mortar and especially at the mortar-stone interface. For all specimens, the masonry breakout failure was characterised by an overlap of the masonry blocks formed along the

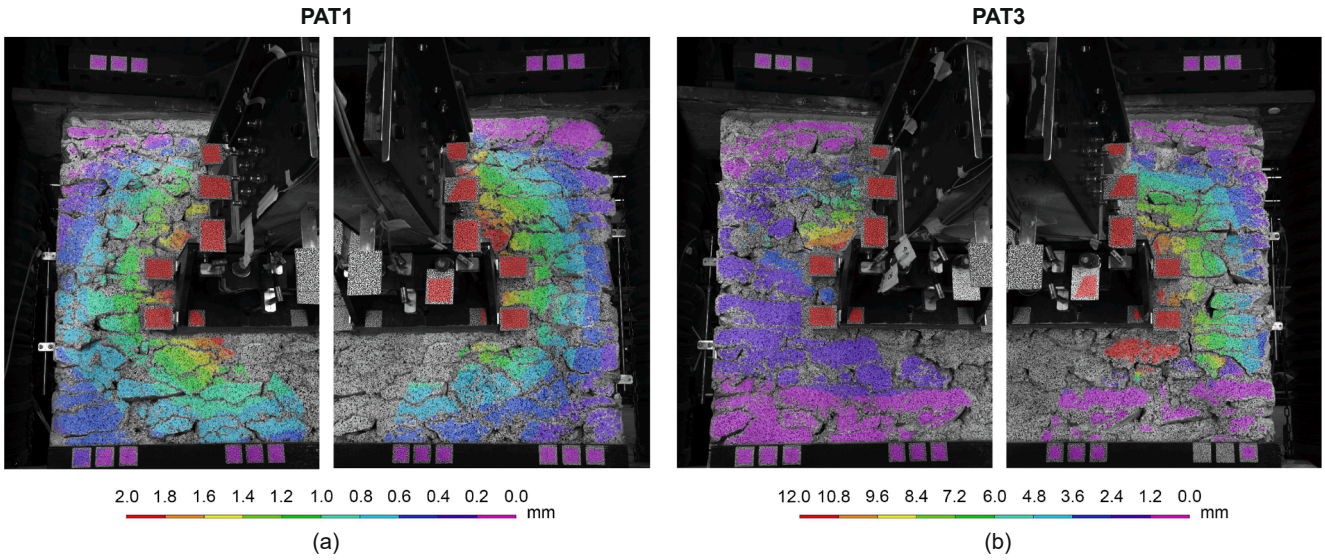

Fig. 14. OOP displacements for PAT specimens at the steps indicated in Fig. 13: (a) PAT1; (b) PAT3.

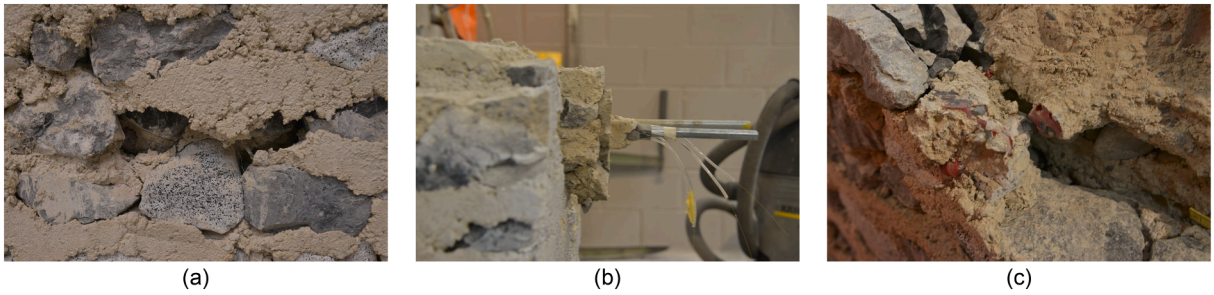

Fig. 15. Damage observed for PAT specimens during demolition: (a) damage at the back of the wall (PAT1); (b) breakout failure (PAT3); (c) damage observed for the anchors (PAT4).

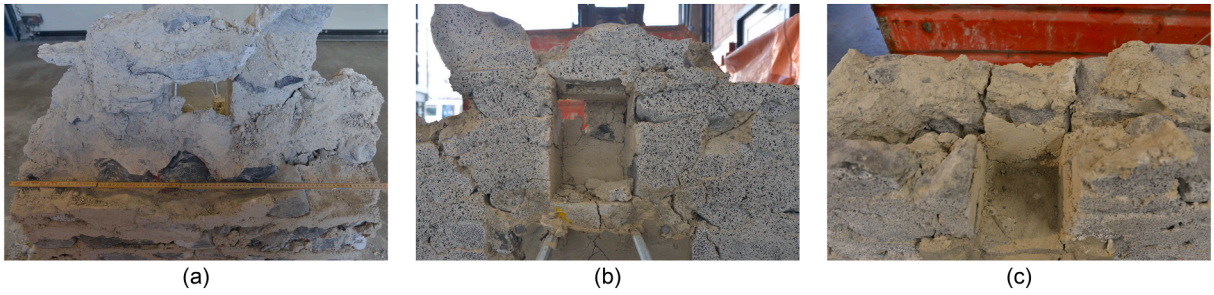

Fig. 16. Common features observed for PAT specimens: (a) top view of the breakout failure (PAT2); (b) damage at the joist pocket (PAT2); (c) cracks behind the joist pocket (PAT4).

length of each anchor. Cracks were also observed between the masonry leaves, especially at mid-height of the walls. In general, these cracks did not significantly propagate up to the external lateral surfaces of the walls, except in specimens IA4, PAT1 and PAT4. This most likely depended on the arrangement and dimensions of the stones at the lateral wall sides.

For PA and IA specimens, no considerable differences were obtained in the angle characterising the geometry of the breakout failure block, especially in the vertical plane (about 45°). In the horizontal plane, the angle ranged between 30 and 60°, depending on the dimensions of the stones as well as on the propagation of cracks between the masonry leaves. When compared to PA specimens, IA specimens with inclined anchors had a masonry breakout block characterised by a smaller depth in the wall but larger dimensions on the wall front surface. As a result, these parameters rather compensate each other when calculating the lateral area of the masonry failure block, which is one of the key parameters governing the peak pull-out force according to existing analytical formulations (see Section 4.1.1). This is presumably why similar values were obtained for the pull-out load capacity in the PA and IA testing series. Regarding the PAT specimens, the breakout failure block also included the masonry portion surrounding the top of the joist pocket. As a result, the lateral area of the failure block did not overall significantly differ from the value obtained for PA specimens, and this is possibly the reason why there was not a significant force reduction.

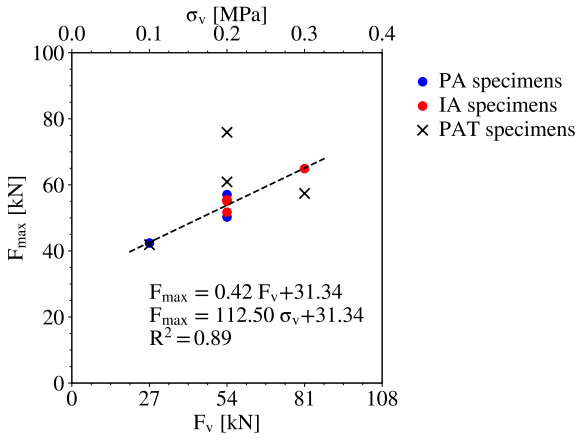

Fig. 17. Peak pull-out force values obtained for the adopted testing configurations under different vertical loading values. Note that the equations and the R^2 value were calculated considering only PA and IA specimens. In the reported equations, F_v must be given in kN, σ_v must be given in N/mm^2 or MPa and F_{max} is obtained in kN.

4. Prediction of pull-out load capacity

In this section, the pull-out load capacity of injection anchors is predicted using currently available formulas in building codes and in the literature. As outlined in Section 1, these formulas were calibrated on results from anchors installed in brick masonry walls. These formulas are therefore used outside their original scope because corresponding equations for injection anchors in stone masonry walls are currently missing. They are used herein to evaluate how the so-obtained predictions compare with the experimental results obtained in this study and to test if they can serve as a starting point for estimating the pull-out capacity of anchors in stone masonry. Because all specimens developed breakout failure, state-of-the-art analytical formulations associated with masonry breakout failure are adopted, as presented in Section 4.1. These formulas apply to straight anchors, so the predicted values are compared with the experimental results obtained for PA specimens. In addition, engineering judgement is used to apply these formulas also to the IA and PAT specimens. In Section 4.2, empirical formulas which have been recently derived to predict the pull-out load capacity of anchors in masonry under breakout failure are applied. Finally, the applicability of these existing formulations is then discussed in Section 4.3.

4.1. Formulas based on analytical models

4.1.1. State-of-the-art analytical formulas

Current analytical formulas for predicting the pull-out load capacity of anchors in masonry have been proposed by using plasticity-based models and models based on the Concrete Capacity Design (CCD) method, which were developed for anchors installed in concrete [40,41]. According to these models, when subjected to tensile loading, the anchor pull-out load resistance for breakout failure depends on the tensile strength of the substrate material (f_t) and the projected area (A^0). The tensile strength is typically expressed in terms of compressive strength (f_m) as $f_t = \kappa_1 \sqrt{f_m}$, where κ_1 is a numerical factor that depends on the unit system adopted. The projected area is assumed as the projection in the pull-out direction of the assumed failure volume on the surface of the element. In the formulas, this becomes $A^0 = \kappa_2 h_{eff}^2$, where h_{eff} is the effective length of the anchor and κ_2 is a constant.

In plasticity-based models, the failure volume is commonly idealised as a cone with an angle of 45°, while in the CCD method, a 35° pyramid is assumed, as shown in Fig. 18. As a result, the projected area for a single anchor under pull-out load corresponds to a circle ($A^0 = \pi h_{eff}^2$) or a square with an edge three times the effective embedment length ($A^0 = 9 h_{eff}^2$). If adjacent anchors are spaced so close together that the failure volumes overlap, or if they are located close enough to a free edge to prevent the full development of the failure volume, a reduction of the load-bearing capacity is considered in both models through a modification factor. This factor is defined as the ratio between the actual projected area of the anchors (A) and the reference projected area for a single anchor not limited by edge or spacing influences (A^0). Among the differences in their formulations, the failure load increases in proportion to the projected area (h_{eff}^2 dependence) in plasticity-based models, while in the CCD method, $h_{eff}^{1.5}$ dependence is assumed for the failure load. This is because the CCD method accounts for size effect by assuming a decrease in the failure load proportional to $\kappa_3 h_{eff}^{-0.5}$, where κ_3 is a numerical factor [40,41].

Consequently, the general expression of the formula to predict the pull-out load capacity (F_{max}^p) associated with breakout failure according to these models can be written as Eq. (1):

$$F_{max}^p = (A/A^0)\kappa\sqrt{f_c}h_{eff}^{\alpha}, \quad (1)$$

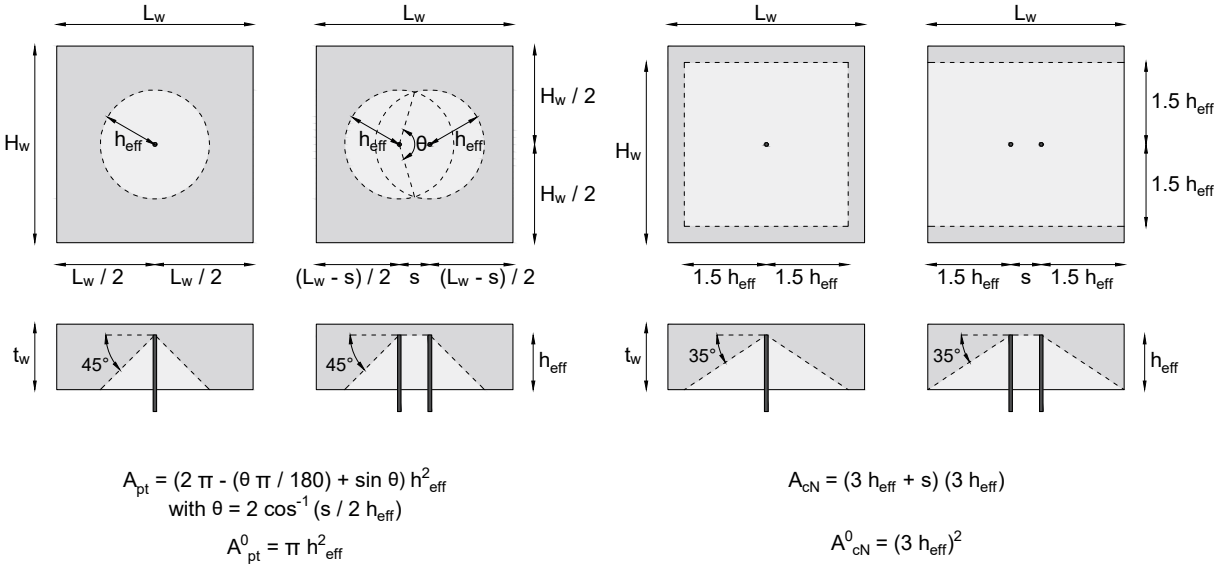

Fig. 18. Schematic representation of the assumed masonry breakout failure blocks and projected areas for PA specimens.

with: $\kappa = \kappa_1 \kappa_2$ and $\alpha = 2.0$, (plasticity-based models)
$\kappa = \kappa_1 \kappa_2 \kappa_3$ and $\alpha = 1.5$. (CCD method).

Table 6 summarises the formulations that have been proposed to calculate the nominal F^p_{max} for anchors installed in masonry under tensile loading. All presented equations are reported in SI units (N and mm), and the same notation is used for parameters reflecting common concepts across the equations, which are the effective length of the anchor (h_{eff}), masonry compressive strength (f_m) and anchor diameter (d). To account for the different shape and angle assumed for the breakout failure volume, the modification factor is expressed in Table 6 as A_{pt}/A^0_{pt} for the plasticity-based models, and A_{cN}/A^0_{cN} for the CCD method.

In Eq. (2) proposed by the MSJC [28], the value of κ_1 is set equal to 0.33, assuming a tensile stress of $f_t = 0.33\sqrt{f_m}$ uniformly distributed over, and acting perpendicular to, the 45° cone lateral surface. This is statically equivalent to $f_t = 0.33\sqrt{f_m}$ uniformly distributed over, and perpendicular to, its projection area. Moreira et al. [33] adapted this formula for stone masonry by considering the κ_1 value to range from 0.08 to 0.33, which was derived from the relationship $f_t = \kappa_1\sqrt{f_c}$ using the results of the characterisation tests carried out by Tomaževič [3]. Specifically, for the pull-out tests by Moreira et al. [33] on bonded grouted anchors in stone masonry, a good correlation was found by adopting $\kappa_1 = 0.10$. Besides falling within the proposed range, this value also agreed with the results obtained from diagonal compression and simple compression tests carried out within the same experimental campaign.

Also based on the theory of plasticity, Arifovic and Nielsen [20] proposed Eq. (4) to estimate the pull-out load capacity for bonded anchors installed in masonry based on work by Hansen et al. [42]. Unlike the other formulas, this equation accounts for the anchor diameter (d). Allen et al. [43] proposed Eq. (5) for headed anchors in masonry, where the factor κ can be assumed to have a value of 7.11 for post-installed anchors in cracked clay brick masonry. For the uncracked condition, as in this case, the load resistance can be increased by a factor of 1.4. It should be noted that this formula is currently the only one based on the CCD method available for anchors in masonry.

4.1.2. Application to experimental tests (PA specimens)

To calculate the pull-out load capacity using the existing analytical formulas, it was assumed from the experimental evidence that the effective length was equivalent to the full embedment length of the anchor (i.e. $h_{eff} = l_e = 250$ mm). For the material properties adopted for masonry, the compressive strength was assumed to be 0.96 MPa, while the tensile strength was assumed to be 0.07 MPa [34] (see Section 2). Using these strength values, the κ_1 factor in Eq. (3) was estimated with a value of 0.08, resulting in the lower-bound limit of the range suggested by Moreira et al. [33]. The projected areas were calculated as shown in Fig. 18. It should be noticed that the overlapping area due to the anchors being closely together was considered, while the edge influence was not considered since the minimum distance requirements were always respected in this case.

Fig. 19 compares the pull-out capacity values estimated via the selected equations (F^p_{max}) and the experimental results (F^e_{max}). To weigh the effectiveness of each formulation, the mean absolute error (MAE) and the mean absolute percentage error (MAPE) are reported in Table 7. The formulas provided by the MSJC [28] and Arifovic and Nielsen [20] predict very similar values for the pull-out load capacity, both overestimating the experimental results. Conversely, Eq. (3) proposed by Moreira et al. [33] significantly underestimates the experimental values. A good correlation could be obtained by adopting a value of $\kappa_1 = 0.22$. Though this κ_1 value is in the proposed range, it is noted that it does not satisfy the relationship between the compressive and tensile strengths of masonry using the results from characterisation tests as proposed by Moreira et al. [33], i.e. $f_t \neq \kappa_1\sqrt{f_m}$ (refer to Section 4.1.1). Equation (5) proposed by Allen et al. [43] correlates better with the experimental results, though the experimental results are still underestimated. This is reflected in Table 7, where this formula reaches the smallest prediction errors. Fig. 19 shows the values obtained for each of the PA specimens when applying Eq. (5). It is noted that Eq. (5) yields the best prediction for PA2, which is the specimen that was subjected to lowest vertical load (0.1 MPa). The reason for the good correspondence might lie in the fact that Eq. (5) does not account for the effect of the vertical load on the pull-out capacity. Neglecting the effect of the vertical load might therefore lead to larger errors for PA3 and PA4, which were subjected to higher vertical loads.

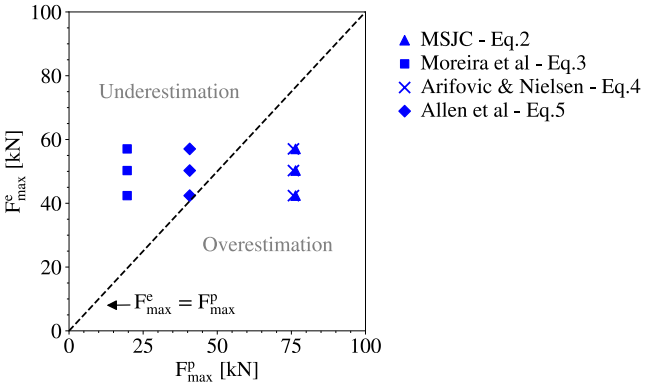

Fig. 19. Comparison between the experimental (F^e_{max}) and predicted (F^p_{max}) values for PA specimens using Eqs. (2)–(5).

4.1.3. Application to experimental tests (IA and PAT specimens)

Based on the experimental evidence, the state-of-the-art analytical formulations were adapted to also predict the pull-out load capacities for IA and PAT specimens using engineering judgment. For the IA specimens, the effective length was assumed to be the length of the anchor in the perpendicular direction of the wall front surface (i.e. $h_{eff} = l_e \cos(\beta) = 230$ mm). To calculate the values of actual projected areas, A_{pt} and A_{cN}, while accounting for the inclination of the anchors, the spacing was redefined as $\hat{s} = s + 2(l_e \sin(\beta))$. Since the critical edge distance was not respected according to the CCD method, a value of $A_{cN} = (2c_1 + \hat{s})(3h_{eff})$ was assumed in Eq. (5), where $c_1 = (L_w - \hat{s})/2$.

For the PAT specimens, when applying Eqs. (2)–(4), the value of A_{pt} was calculated by subtracting the overlapping area of the joist pocket in the reference projected area A^0_{pt}. According to the CCD method, a value of $A_{cN} = (3h_{eff})(1.5h_{eff} + s + c_2)$ could be adopted for Eq. (5),

Table 6
Summary of formulas available to determine the breakout force capacity of anchors in masonry. Note that f_m must be given in N/mm^2 or MPa, dimensions must be given in mm and F^p_{max} is obtained in N.

Author	Formulas	
MSJC (2016) [28]	$F^p_{max} = \left(A_{pt}/A^0_{pt}\right) 0.33\,\pi\sqrt{f_m}\,h^2_{eff}$	(2)
Moreira et al. (2016) [33]	$F^p_{max} = \left(A_{pt}/A^0_{pt}\right) \kappa_1\,\pi\sqrt{f_m}\,h^2_{eff}$ with $0.08 \leq \kappa_1 \leq 0.33$	(3)
Arifovic & Nielsen (2006) [20]	$F^p_{max} = \left(A_{pt}/A^0_{pt}\right) 0.96\sqrt{f_m}\,h^2_{eff}(1 + d/h_{eff})$	(4)
Allen et al. (2000) [43]	$F^p_{max} = 1.4\left[\left(A_{cN}/A^0_{cN}\right) 7.11\sqrt{f_m}\,h^{1.5}_{eff}\right]$	(5)

Table 7
Values of MAE and MAPE obtained using Eqs. (2)–(5).

Author	MAE [kN]	MAPE [-]
MSJC (2016) [28] - Eq. (2)	26.4	0.55
Moreira et al. (2016) [33] - Eq. (3)	30.3	0.60
Arifovic & Nielsen (2006) [20] - Eq. (4)	25.7	0.54
Allen et al. (2000) [43] - Eq. (5)	9.3	0.17

assuming c_2 as the distance between the anchors and the joist pocket. However, this requirement was found to be too conservative to account for the presence of the joist pocket, so the value of A_{cN} was computed following the same approach used as previously (i.e. by subtracting the overlapping area of the joist pocket in the reference projected area A^0_{cN}).

As shown in Fig. 20, when compared to PA specimens, higher values of F^p_{max} were calculated for IA specimens using Eqs. (2)–(4). For IA specimens, though a lower projected area was obtained for each anchor due to the inclination of the anchors, a higher ratio A_{pt}/A^0_{pt} was calculated as the overlapping area was reduced. Because the pull-out load capacity was reduced to respect minimum edge distance requirements, the value obtained for IA specimens using Eq. (5) is very similar to that obtained for PA specimens. For the PAT specimens, all adopted equations predicted lower pull-out load capacity values when compared to PA specimens as a direct result of considering the overlap with the area of the joist pocket. It is to be noted that PAT2 and PAT4 were neglected here due to the probable influence of existing damage and crack repair for these specimens (refer to Section 3.4).

4.2. Empirical formulas

Recently, Ceroni et al. [12,44] proposed formulas for predicting the pull-out load capacity of anchors installed in stone and brick masonries using regression analysis. Specifically, they were calibrated based on a database including pull-out tests for which the masonry breakout failure was also observed. According to the notation previously introduced, the formulas, expressed in N and mm, can be written as follows:

$$F^p_{max} = k\,\alpha\left(\frac{d}{d_0}\right)^{\beta} l_e^{\gamma}\, d_0^{\delta}\, 0.25\, f_{cg}^{\varepsilon}, \tag{6}$$

$$F^p_{max} = k\left[\alpha\,\frac{(0.67\,f_t + 0.4\,\sigma_v)^{\beta}}{f_m^{\theta}} + \gamma\, d_0^{\delta}\, l_e^{\varepsilon}\,(0.67\,f_t + 0.4\,\sigma_v)^{\eta}\right]. \tag{7 and 8}$$

In all formulations, the pull-out load capacity depends on the geometry of the anchor. Equation (6) depends on the compressive strength of the injection material (f_{cg}), while the compressive and tensile strengths of masonry are adopted in Eqs. (7) and (8). Notably, Eqs. (7) and (8) include the effect of overburden stress in the term $(0.67\,f_t + 0.4\,\sigma_v)$, adopted according to the Mohr-Coulomb criterion. Eq. (7) was calibrated based on only the tests which failed involving the masonry, while Eq. (8) accounted for all the collected pull-out tests independently on the failure mode. The parameters α, β, γ, δ, ε, η, θ and κ are numerical factors obtained from regression analysis by Ceroni et al. [12,44]. For the reader's convenience, the values obtained for these parameters for Eqs. (6)–(8) are reported in Table 8.

All the experimental results considered in the adopted database were obtained from pull-out tests on straight anchors, then the formulations were adopted to predict the pull-out load capacity for PA specimens. As the database also included the pull-out tests carried out on pairs of anchors by Moreira et al. [11], the modification factor A/A^0 was not applied here. The f_{cg} value was adopted to be 82.7 MPa according to the manufacturer's specifications. For the values of masonry material properties, they were assumed as mentioned above, i.e. $f_m = 0.96$ MPa and $f_t = 0.07$ MPa.

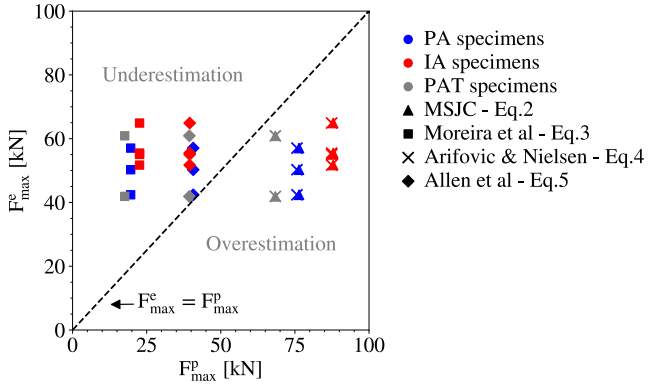

Fig. 20. Comparison between the experimental (F^e_{max}) and predicted (F^p_{max}) values for all testing series using Eqs. (2)–(5).

The results obtained by comparing the values predicted by Eqs. (6)–(8) with the experimental results are presented in Fig. 21 and Table 9. Accounting also for the influence of overburden stress, Eqs. (7) and (8) are better at predicting the experimental values. When compared to Eq. (7), Eq. (8) shows lower values of MAE and MAPE (6.2 kN and 0.13, respectively), possibly as it was calibrated on a larger set of experimental results. However, it is to be noted that when applying Eqs. (7) and (8), the predicted value obtained for $\sigma_v = 0.20$ MPa is lower than the value calculated for $\sigma_v = 0.10$ MPa (Fig. 21), which is in contradiction to the trends observed in experimental results. This might be due to the fact that, as a result of the lack of experimental data in literature, the adopted database included a limited number of tests which failed for masonry breakout and where the overburden stress was varied.

4.3. Discussion

In this section, seven existing formulas for estimating the peak pull-out force of anchors in masonry under breakout failure were applied to the tests presented in Section 3. Of these equations, four were analytical equations (Eqs. (2)–(5)), and three were empirical equations (Eqs. (6)–(8)). The existing analytical equations had been developed for anchor breakout failure from concrete, and then the parameters had been recalibrated for brick masonry. The only previous attempt to extend the application of these formulas to stone masonry was done by Moreira et al. [33], who proposed a range of the κ_1 value from 0.08 to 0.33 to the analytical formula for the breakout load capacity of anchors. With the exception of the equation by Moreira et al. [33], the predictive analytical equations were therefore applied out of their original scope. The comparison had therefore not the goal to highlight any shortfalls of these equations but to investigate their potential for future work when deriving specific equations for the pull-out force capacity of anchors in stone masonry under breakout failure.

The comparison of the formulas to the three test series presented in this paper yielded the following insights:

- Parallel anchors (PA): The predicted pullout capacities differed significantly from the experimental pull-out values. This also applies to the one equation that had been calibrated for stone masonry (i.e. Eq. (3)). Two out of the four analytical equations underestimated the capacities, while the other two overestimated the capacities. All four equations have in common that they do not account for the overburden stress and could therefore not capture the trends in the PA data. Two empirical equations, i.e. Eqs. (7) and (8), accounted for the overburden stress. However, the predicted values were lower for $\sigma_v = 0.20$ MPa than for $\sigma_v = 0.10$ MPa, which is contrary to the trend observed from the experiments. This might be related to the fact that these equations are purely empirical and only few of the tests used for the calibration had been carried out with an overburden stress. Nevertheless, Eq. (8) by Ceroni et al. [12] led to the overall best predictions of the pull-out capacity.
- Inclined anchors (IA) and parallel anchors with timber beam (PAT): The existing analytical equations were not addressing inclined anchors or parallel anchors with a joist pocket. We extended their application to these configurations by modifying geometric input quantities using the experimental observations and engineering judgment; the reflections are described in detail in Sections 4.1.2 and 4.1.3. With the proposed modifications, the formulas available for parallel anchors may be successfully adapted to these configurations by modifying the geometric input quantities of the anchoring system.

Table 8
Values of parameters obtained for Eqs. (6)–(8) by Ceroni et al. [12,44].

Author	α	β	γ	δ	ε	η	θ	κ
Ceroni et al. (2020) [44] - Eq. (6)	282	0.40	1.05	0.24	0.08	–	–	1.00
Ceroni et al. (2020) [12] - Eq. (7)	189.189	1.51	0.48	−0.36	2.10	−0.44	0.50	1.00
Ceroni et al. (2020) [12] - Eq. (8)	191.059	1.41	0.38	−0.37	2.11	−0.49	0.50	1.00

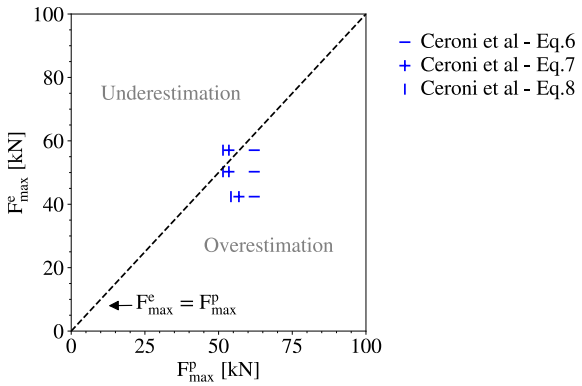

Fig. 21. Comparison between the experimental (F^e_{max}) and predicted (F^p_{max}) values for PA specimens using Eqs. (6)–(8).

Table 9
Values of MAE and MAPE obtained using Eqs. (6)–(8).

Author	MAE [kN]	MAPE [-]
Ceroni et al. (2020) [44] - Eq. (6)	12.1	0.26
Ceroni et al. (2020) [12] - Eq. (7)	7.1	0.16
Ceroni et al. (2020) [12] - Eq. (8)	6.2	0.13

Using the quantities of the configurations adopted in this study, the predicted pull-out load values for the IA and PAT specimens did not differ significantly from those calculated for the PA specimens. This agrees with the experimental results, as IA and PAT specimens led to overall similar pull-out force capacities to PA specimens in this study. Hence, it seems that the formulas available for parallel anchors might be successfully adapted following the herein proposed engineering approach. However, because the prediction of the pull-out load was unsatisfactory for the specimens with parallel anchors, low agreement between the predicted and experimental values was also obtained for IA and PAT specimens.

To sum up, it seems necessary to expand the analytical formulas by a term that accounts for the overburden stress. If done so, based on the results obtained, it seems feasible to extend the applications also to the configurations of the IA and PAT tests. While the empirical formula which accounts for the overburden stress led to the best prediction, it does not yet reproduce correctly the positive correlation between overburden stress and pullout load capacity but instead suggests a weak negative correlation.

5. Concluding remarks

This paper presented the results of twelve quasi-static pull-out tests performed to investigate the behaviour of injected anchors in stone masonry. Each specimen implemented an anchoring system with two steel rods injected in a double-leaf stone masonry wall using epoxy resin adhesive. Three testing configurations were adopted: 1) PA specimens with parallel anchors; 2) IA specimens with anchors inclined in the horizontal plane; and 3) PAT specimens with parallel anchors and a joist pocket in the masonry. The main findings of the paper are summarised as follows:

- Before the maximum pull-out force was reached, the obtained experimental force–displacement response curves were nearly linear, and no damage was visible on the wall surfaces. The peak force was achieved at a relatively low displacement, resulting in a rather stiff systemic response in the pre-peak branch. In the post-peak behaviour, cracks rapidly propagated in the masonry walls, and a significant decrease in force was observed. This behaviour was associated with masonry breakout failure, which was obtained for all specimens as intended. On the wall front surface, cracks developed around the anchoring system and propagated outwards, occurring mainly in mortar joints and at the mortar-stone interface. In the wall thickness, masonry blocks formed around each anchor along the full anchor length, and they overlapped as a result of their proximity. In addition, cracks were found between the masonry leaves, suggesting their separation in the area surrounding the anchoring system.
- This experimental programme investigated the effect of anchoring detail, vertical overburden stress and the presence of a joist pocket in the masonry. No significant effect of the anchoring detail was found on the peak pull-out force in this study. When considering PA and IA specimens tested under an overburden stress of 0.20 MPa, the mean pull-out load capacity was calculated to be 53.9 kN (CoV = 5 %). The overburden stress applied to the masonry walls considerably influenced the peak pull-out force, which was clear for the specimens with parallel and inclined anchors where the peak pull-out load increased with increasing overburden stress. Finally, there is some indication that the joist pocket did not drastically influence the pull-out load capacity in this study; however, further investigations are needed to form solid conclusions of its effect.
- Being aware of limitations, current state-of-the-art formulations for predicting the pull-out force capacity of anchors in masonry were applied to be tested with the experimental results obtained in this study. As they were derived for straight anchors, these formulas were straightforwardly used to predict the pull-out load capacity values obtained from PA specimens. Moreover, they were also applied with engineering judgement to predict the results from IA and PAT specimens. When using existing analytical formulations, unsatisfactory results were obtained by comparing the predicted and the experimental values of pull-out force capacity. Better agreement was shown by the empirical formula derived by Ceroni et al. [12] that allows to predict the pull-out load capacity of anchors in masonry accounting for the effect of overburden stress. However, it failed in predicting the relationship observed in this study between pull-out load capacity and overburden stress.

The results obtained in this paper underline the need for an analytical formulation that also includes the overburden stress as a governing parameter when estimating the pull-out load capacity of anchors in masonry under breakout failure. Considering the lack in literature of results obtained from pull-out tests on injection anchors in rubble stone masonry, as well as the large variation in experimental results typically affecting this masonry typology due to several factors (e.g. the great variability in size, shape and material properties of masonry constituents), more laboratory and *in-situ* tests should be addressed in future work to confirm and extend the results obtained in this experimental programme. The experimental results reported in this paper can serve for numerical simulations of stone masonry buildings where wall-to-diaphragm connections are reinforced by injection anchors. Moreover, they can validate the simulation of pull-out tests on detailed micro-

models of stone masonry walls (e.g. [45,46]), which can be used to evaluate the effect of the above-mentioned factors and to investigate scenarios not explicitly considered in the context of this article.

CRediT authorship contribution statement

Maria Pia Ciocci: Methodology, Validation, Formal analysis, Investigation, Data curation, Writing – original draft, Writing – review & editing, Visualization. **Serena van Nimwegen:** Methodology, Writing – review & editing. **Arash Askari:** Investigation, Data curation, Writing – review & editing, Visualization. **Francesco Vanin:** Methodology, Investigation, Writing – review & editing. **Paulo B. Lourenço:** Writing – original draft, Writing – review & editing, Supervision. **Katrin Beyer:** Conceptualization, Methodology, Validation, Resources, Writing – original draft, Writing – review & editing, Supervision, Project administration, Funding acquisition.

Declaration of Competing Interest

The authors declare that they have no known competing financial interests or personal relationships that could have appeared to influence the work reported in this paper.

Data availability

Data will be made available on request.

Acknowledgments

The support of this project by the Swiss Federal Office for the Environment, FOEN, in the framework of the action plan timber (“Aktionsplan Holz’’) as well as by Lignum Holzwirtschaft Schweiz is gratefully acknowledged. The first author was partly supported by the Portuguese Foundation for Science and Technology (FCT) within the INFRARISK PhD program (PD/BD/127910/2016). The authors would also like to thank the team of the Structural Engineering Laboratory at EPFL for their help with the planning and execution of the tests, namely Gilles Guignet, Serge Despont, Armin Krkic, Gérald Rouge, Frédérique Dubugnon and François Perrin.

References

[1] D’Ayala DF, Paganoni S. Assessment and analysis of damage in L’Aquila historic city centre after 6th April 2009. Bull Earthq Eng 2011;9:81–104. https://doi.org/10.1007/s10518-010-9224-4.
[2] Penna A, Morandi P, Rota M, Manzini CF, da Porto F, Magenes G. Performance of masonry buildings during the Emilia 2012 earthquake. Bull Earthq Eng 2014;12:2255–73. https://doi.org/10.1007/s10518-013-9496-6.
[3] Tomaževič M. Earthquake-resistant design of masonry buildings. 1st ed. London, United Kingdom: Imperial College Press; 1999.
[4] Bruneau M. State-of-the-art report on seismic performance of unreinforced masonry buildings. J Struct Eng 1994;120:230–51. https://doi.org/10.1061/(ASCE)0733-9445(1994)120:1(230).
[5] Sorrentino L, D’Ayala D, de Felice G, Griffith MC, Lagomarsino S, Magenes G. Review of out-of-plane seismic assessment techniques applied to existing masonry buildings. Int J Archit Herit 2016;11:1–20. https://doi.org/10.1080/15583058.2016.1237586.
[6] Almeida JP, Beyer K, Brunner R, Wenk T. Characterization of mortar–timber and timber–timber cyclic friction in timber floor connections of masonry buildings. Mater Struct 2020;53:51. https://doi.org/10.1617/s11527-020-01483-y.
[7] Wenk T, Brunner R, Pacheco de Almeida J, Beyer K. Überprüfung bezüglich Erdbeben von Holzbalkendecken in Bestandesbauten (Seismic assessment of existing buildings with timber floors). Der Bauingenieur 2020;95(04):S 8–13.
[8] Vanin F, Penna A, Beyer K. Equivalent-frame modeling of two shaking table tests of masonry buildings accounting for their out-of-plane response. Front Built Environ 2020;6:1–18. https://doi.org/10.3389/fbuil.2020.00042.
[9] Tomić I, Vanin F, Božulić I, Beyer K. Numerical simulation of unreinforced masonry buildings with timber diaphragms. Buildings 2021;11:205. https://doi.org/10.3390/buildings11050205.
[10] Paganoni S, D’Ayala D. Testing and design procedure for corner connections of masonry heritage buildings strengthened by metallic grouted anchors. Eng Struct 2014;70:278–93. https://doi.org/10.1016/j.engstruct.2014.03.014.
[11] Moreira S, Ramos LF, Oliveira DV, Lourenço PB. Experimental behavior of masonry wall-to-timber elements connections strengthened with injection anchors. Eng Struct 2014;81:98–109. https://doi.org/10.1016/j.engstruct.2014.09.034.
[12] Ceroni F, Di Ludovico M. Traditional and innovative systems for injected anchors in masonry elements: experimental behavior and theoretical formulations. Constr Build Mater 2020:254. https://doi.org/10.1016/j.conbuildmat.2020.119178.
[13] Contrafatto L, Cosenza R. Behaviour of post-installed adhesive anchors in natural stone. Constr Build Mater 2014;68:355–69. https://doi.org/10.1016/j.conbuildmat.2014.05.099.
[14] Porcarelli S, Shedde D, Wang Z, Ingham JM, Giongo I, Dizhur D. Tension and shear anchorage systems for limestone structures. Constr Build Mater 2021;272:121616. https://doi.org/10.1016/j.conbuildmat.2020.121616.
[15] Dizhur D, Schultz A, Ingham J. Pull-out behavior of adhesive connections in unreinforced masonry walls. Earthq Spectra 2016;32:2357–75. https://doi.org/10.1193/011115EQS006M.
[16] ICOMOS and ISCARSAH. Recommendations for the analysis, conservation and structural restoration of architectural heritage. France, Charenton-Le-Pont: International Council of Monuments and Sites (ICOMOS); 2003.
[17] Dizhur D, Ismail N, Knox C, Lumantarna R, Ingham JM. Performance of unreinforced and retrofitted masonry buildings during the 2010 Darfield earthquake. Bull New Zeal Soc Earthq Eng 2010;43:321–39. https://doi.org/10.5459/bnzsee.43.4.321-339.
[18] Moon L, Dizhur D, Senaldi I, Derakhshan H, Griffith M, Magenes G, et al. The demise of the URM building stock in Christchurch during the 2010–2011 Canterbury earthquake sequence. Earthq Spectra 2014;30:253–76. https://doi.org/10.1193/022113EQS044M.
[19] Gigla B. Bond strength of injection anchors as supplementary reinforcement inside historic masonry. In: 13th Int. Brick Block Conf., Amsterdam; 2004. p. 119–28.
[20] Arifovic F., Nielsen M.P. Strength of anchors in masonry. Report BYG DTU, R-134; 2006.
[21] Silveri F, Riva P, Profeta G, Poverello E, Algeri C. Experimental study on injected anchors for the seismic retrofit of historical masonry buildings. Int J Archit Herit 2016;10:182–203. https://doi.org/10.1080/15583058.2015.1113333.
[22] Muñoz R, Lourenço PB. Mechanical behaviour of metal anchors in historic brick masonry: an experimental approach. In: Aguilar R, Torrealva D, Moreira S, Pando MA, Ramos LF, editors. Struct. Anal. Hist. Constr., RILEM Bookseries, 18. Cham, Germany: Springer; 2019. p. 788–98. https://doi.org/10.1007/978-3-319-99441-3_85.
[23] Giresini L, Puppio ML, Taddei F. Experimental pull-out tests and design indications for strength anchors installed in masonry walls. Mater Struct 2020;53:103. https://doi.org/10.1617/s11527-020-01536-2.
[24] Burton C, Visintin P, Griffith M, Vaculik J. Field testing of vintage masonry: Mechanical properties and anchorage strengths. Structures 2020;28:1900–14. https://doi.org/10.1016/j.istruc.2020.10.023.
[25] Ismail N. Performance of wall to diaphragm anchors for use in seismic upgrade of heritage masonry buildings. Int J Archit Herit 2016;10:829–40. https://doi.org/10.1080/15583058.2016.1144115.
[26] Muñoz R, Lourenço PB, Moreira S. Experimental results on mechanical behaviour of metal anchors in historic stone masonry. Constr Build Mater 2018;163:643–55. https://doi.org/10.1016/j.conbuildmat.2017.12.090.
[27] Ceroni F, Cuzzilla R, Pecce M. Assessment of performance of steel and GFRP bars as injected anchors in masonry walls. Constr Build Mater 2016;123:78–98. https://doi.org/10.1016/j.conbuildmat.2016.06.124.
[28] MSJC. TMS 402/602-16 building code requirements and specification for masonry structures; 2016.
[29] McGinley WM. Design of anchor bolts in masonry. Prog Struct Eng Mater 2006;8:155–64. https://doi.org/10.1002/pse.222.
[30] EOTA. European assessment document EAD 330076-00-0604: metal injection anchors for use in masonry; 2014.
[31] EOTA. Technical report TR 053: recommendations for job-site tests of metal injection anchors for use in masonry; 2016.
[32] EOTA. Technical Report TR 054: design method for anchorages with metal injection for use in masonry; 2016.
[33] Moreira S, Ramos LF, Oliveira DV, Lourenço PB. Design parameters for seismically retrofitted masonry-to-timber connections: injection anchors. Int J Archit Herit 2015;10. https://doi.org/10.1080/15583058.2015.1113339.
[34] Rezaie A, Godio M, Beyer K. Experimental investigation of strength, stiffness and drift capacity of rubble stone masonry walls. Constr Build Mater 2020;251:118972. https://doi.org/10.1016/j.conbuildmat.2020.118972.
[35] Vintzileou E, Miltiadou-Fezans A. Mechanical properties of three-leaf stone masonry grouted with ternary or hydraulic lime-based grouts. Eng Struct 2008;30:2265–76. https://doi.org/10.1016/j.engstruct.2007.11.003.
[36] Silva RA, Domínguez-Martínez O, Oliveira DV, Pereira EB. Comparison of the performance of hydraulic lime- and clay-based grouts in the repair of rammed earth. Constr Build Mater 2018;193:384–94. https://doi.org/10.1016/j.conbuildmat.2018.10.207.
[37] EN 1015-11. Methods of test for mortar for masonry – part 11: determination of flexural and compressive strength of hardened mortar. Brussels, Belgium: European Standards, CEN/TC; 1999.
[38] ASTM D7012-14e1. Standard test methods for compressive strength and elastic moduli of intact rock core specimens under varying states of stress and temperatures. West Conshohocken, PA, USA: ASTM Standard, ASTM International; 2014. doi: 10.1520/D7012-14E01.
[39] Correlated solutions, VIC-3D software manual; 2020.
[40] Fuchs W, Eligehausen R, Breen JW. Concrete capacity design (CCD) approach for fastening to concrete. ACI Struct J 1995;92.

[41] Eligehausen R, Mallée R, Silva JF. Anchorage in concrete construction. Berlin, Germany: Ernst & Sohn; 2016.
[42] Hansen L.Z., Findsen K., Nielsen M.P. Beregning af indlimede ankre i murede vaegge (Strength of bonded anchors in masonry) Report BYG DTU, R-085. 2004.
[43] Allen R, Borchelt JG, Klingner RE, Zobel R. Proposed provisions for design of anchorage to masonry. TMS J 2000.
[44] Ceroni F, Di Ludovico M, Balsamo A. Effectiveness of design formulations for injected anchors in masonry elements. J Build Pathol Rehabil 2020;5(1). https://doi.org/10.1007/s41024-020-0077-1.
[45] Zhang S, Hofmann M, Beyer K. A 2D typology generator for historical masonry elements. Constr Build Mater 2018;184:440–53. https://doi.org/10.1016/j.conbuildmat.2018.06.085.
[46] Shaqfa M, Beyer K. A virtual microstructure generator for 3D stone masonry walls. Eur J Mech - A/Solids 2022;96:104656. https://doi.org/10.1016/j.euromechsol.2022.104656.